



Universidad Autónoma
de Madrid

Biblos-e Archivo
Repositorio Institucional UAM

Repositorio Institucional de la Universidad Autónoma de Madrid

<https://repositorio.uam.es>

Esta es la **versión de autor** del artículo publicado en:
This is an **author produced version** of a paper published in:

Journal of Industrial and Engineering Chemistry 82 (2020): 317-323

DOI: <https://doi.org/10.1016/j.jiec.2019.09.024>

Copyright: © 2019 The Korean Society of Industrial and Engineering Chemistry. Published by Elsevier B.V.

El acceso a la versión del editor puede requerir la suscripción del recurso
Access to the published version may require subscription

Pursuit of Optimal Synthetic Conditions for Obtaining Colloidal Zero-Valent Iron Nanoparticles by Scanning Pulsed Laser Ablation in Liquids

*Ruth Lahoz,¹ Eva Natividad,^{**2} Álvaro Mayoral,³ Christian Rentenberger,⁴ Daniel Díaz-Fernández,⁵ Eduardo J. Félix,⁶ Leonardo Soriano,⁵ Wolfgang Kautek,⁷ Oscar Bomati-Miguel.^{*5,6}*

1. Centro de Química y Materiales de Aragón (CEQMA), CSIC-Universidad de Zaragoza. Campus Rio Ebro, 50018 Zaragoza, Spain. rlahoz@unizar.es.
2. Instituto de Ciencia de Materiales de Aragón (ICMA), CSIC-Universidad de Zaragoza. EINA, Edificio Torres Quevedo, María de Luna, 3, 50018 Zaragoza, Spain. evanat@unizar.es.
3. Centre for High-resolution Electron Microscopy (ChEM), School of Physical Science and technology, ShanghaiTech University. 393 Middle Huaxia Road, Pudong, Shanghai, 201210, China. amayoral@shanghaitech.edu.cn
4. Faculty of Physics, University of Vienna. Boltzmanngasse 5, 1090 Vienna, Austria. christian.rentenberger@univie.ac.at
5. Departamento de Física Aplicada. Facultad de Ciencias, Universidad Autónoma de Madrid. Campus de Cantoblanco, 28049 Madrid, Spain. Dr. Díaz-Fernández (daniel.diaz@paralab.es), Prof. Dr. L. Soriano (l.soriano@uam.es)
6. Departamento de Física de la Materia Condensada and Institute of Research on Electron Microscopy and Materials (IMEYMAT). Universidad de Cádiz. Campus Universitario Polígono Río San Pedro, 11510 Puerto Real, Cádiz, Spain. Ph.D. student E. J. Félix (edu25794@gmail.com), Dr. O Bomati-Miguel (oscar.bomati@uca.es)
7. Department of Physical Chemistry, University of Vienna. Waehringer Strasse 42, 1090 Vienna, Austria. wolfgang.kautek@univie.ac.at

* Corresponding author.
Dr. Oscar Bomati Miguel
E-mail address: oscar.bomati@uca.es

** Co-corresponding author.
Dr. Eva Natividad
E-mail address: evanat@unizar.es

ABSTRACT

Liquid-Assisted Pulsed Laser Ablation (LA-PLA) is a promising top-down method to directly synthesize colloidal dispersions of nanoparticles in a eco-friendly manner. However, the role of LA-PLA synthesis parameters is not yet fully agreed. This work seeks to optimize the production of nanoscale zero-valent iron (nZVI) particles suitable for biomedical or environmental applications using nanosecond LA-PLA on iron targets with different ablation media, laser and target scanning parameters. The use of alcohols as solvents produces iron-iron oxide core-shell nanoparticles with amorphous cores, except for a small crystalline fraction corresponding to the biggest core sizes. Decreasing carbon chain length and complexity leads to a thinning of the carbonaceous material coatings and an increase of the colloidal stability and the nanoparticle productivity. Moreover, a decrease of solvent density and surface tension allows obtaining reduced sizes and polydispersity values. Among, laser and scanning parameters, the pulse accumulation per spot displayed a clear effect in boosting size and productivity. As main outcome, aqueous dispersions with suitable colloidal properties are obtained, either by transferring to water of optimized nZVI particles produced in ethanol, or by direct formation of nZVI particles and in situ coating with hydrophilic molecules in aqueous solutions of these molecules.

KEYWORDS: Nanoscale zero-valent iron particles; Core-shell structure, Water-stable colloidal metal nanoparticles; Surface functionalization; Liquid-assisted nanosecond pulsed laser ablation; High-resolution transmission electron microscopy.

1. Introduction

Magnetic nanoscale zero-valent iron particles (nZVI) exhibit a core-shell structure, where an Fe(II)/Fe(III) oxide-oxyhydroxide shell protects a Fe^0 core from rapid oxidation. ZVI nanoparticles have been intensely investigated in recent years, mainly because of their potential biomedical applications, such as contrast enhancement for magnetic resonance imaging, and magnetic hyperthermia treatments. [1] There are numerous reasons for this interest in these nanoparticle colloids. nZVI particles can be coated with hydrophilic molecules to improve their colloidal stability in aqueous solutions and their circulation time in blood. Also, they show higher saturation magnetization and initial susceptibility than paramagnetic compounds (gadolinium III chelates) and commercial colloidal dispersions of superparamagnetic iron oxide nanoparticles (SPIONs), which are currently used in medical applications. Moreover, recent studies have reported that these nanoparticles exhibit a stronger antimicrobial activity. [2] Beyond biomedical applications, nZVI particles show higher adsorption and reactivity capacities for contaminants degradation than larger, granular zero-valent iron particles, which are used traditionally in permeable reactive barriers for in situ treatment of polluted sites. This is due to the reducing activity of their Fe^0 core, their larger surface area, and the presence of a high density of sites for chemical reactions in their oxide shell. [3] This, together with their small size, allows direct injection of colloidal dispersions of nZVI particles into polluted sites, where they remain in suspensions for a long time, providing an in situ treatment and stabilization of emanating plumes. [4]

Benefits of using nZVI particles in medicine and environmental applications are evident. Therefore, the development of efficient synthesis methods to meet the demand of these

nanoparticles is under intense research. Traditionally, nZVI particles have been synthesized at laboratory scale by bottom-up approaches. They involve methods either in aqueous media (*e.g.* coprecipitation [5]) or in organic media (*e.g.* sonochemical or thermally induced decomposition of iron organic precursors [6]). These methods produce more or less homogeneous nZVI particles with high reactivity. However, they suffer from serious drawbacks for large-scale manufacturing, partially due to the necessity of applying large quantities of expensive surfactants and/or several synthetic steps to control the size, aggregation and colloidal stability of the synthesized nanoparticles. Moreover, they produce large amounts of intermediate products and impurities in the final nZVI particles, making necessary multiple purification processes, increasing the fabrication costs and waste production. Laboratory scale production of nZVI particles has also been achieved by gas phase techniques, *e.g.*, gas condensation of iron vapors under inert atmospheres, [7] laser pyrolysis [8] and laser ablation. [9] However, they produce agglomerated nanoparticles that have to be subjected to expensive processes for their dispersion in aqueous media. On the other hand, top-down large-scale manufacturing of nZVI particles has been achieved by mechanical grinding of granular bulk iron. [10] However, the nanoparticles synthesized by this method suffer from severe aggregation, poor size and shape control, and the necessity to apply additional processes for achieving water dispersions.

Recently, **LA-PLA** has been identified as a promising alternative top-down method to synthesize directly colloidal dispersions of nanoparticles (NPs), because of its low cost, simplicity, and environmental friendliness. [11] This technique consists in the ablation of bulk materials immersed inside the required solvent by using a pulsed laser. This simple set-up allows the generation of high purity metal nanoparticles colloids (Ag, Au, Ge, Pt, Pd, Cu, Fe, Co, Ni, Zn, Si, Al...) stable in different liquids as a function of their application requirements. [12] With this

1
2
3
4 method, chemical precursors are replaced by much cheaper bulk raw materials and the use of
5
6 stabilizing molecules is not imperative. This enables to reduce waste generation and operational
7
8 costs. Moreover, continuous production with scale-up productivity can be achieved by using
9
10 liquid flow systems in combination with the use of high repetition nanosecond pulsed lasers
11
12 equipped with surface scanning systems. [13]
13
14

15
16
17 In particular, colloidal dispersions of nZVI particles have been synthesized by
18
19 nanosecond/femtosecond laser ablation of bulk iron targets submerged in different organic
20
21 solvents. [11a,14] These nanoparticles showed different size, crystallinity and shell composition
22
23 as a function of the nature of the solvent used. However, the correct election of the processing
24
25 parameters for an optimum performance of LA-PLA to fabricate nZVI particles remains a
26
27 challenge. This is because the nanoparticle generation into the liquid takes place through a series
28
29 of complex mechanisms extended over many orders of magnitude, namely, local surface melting,
30
31 thermal evaporation, plasma plume generation, plasma expansion inside a gas bubble and
32
33 ejection of molten droplets, nucleation and growth of nanoparticles within the plume, penetration
34
35 of condensed nano-sized phases into the liquid, but also secondary beam-colloid interaction.
36
37 These mechanisms are largely driven by the nature of the bulk target and solvent used, and the
38
39 imposed laser irradiation conditions (*e.g.* pulse width or wavelength,). [11c, 15] Unfortunately,
40
41 the impact of these parameters on the characteristics of the synthesized nanoparticles is not yet
42
43 agreed upon within the scientific community. This lack of information is especially significant in
44
45 the case of the oxidized core-shell iron nanoparticles, where the possible candidates for the iron-
46
47 oxide phases are numerous (FeO , $\alpha\text{-Fe}_2\text{O}_3$ (hematite), $\gamma\text{-Fe}_2\text{O}_3$ (maghemite), Fe_3O_4 (magnetite),
48
49 and $\alpha\text{-FeO(OH)}$ (goethite)), and whose presence could modify their biocompatibility and
50
51 colloidal, magnetic and catalytic properties.
52
53
54
55
56
57
58
59
60
61
62
63
64
65

1
2
3
4 In order to overcome this lack of consensus, a systematic investigation of the influence of the
5
6 different laser parameters on the productivity, size, polydispersity, structure, crystallinity and
7
8 composition of the nZVI particles generated by liquid-assisted pulsed laser ablation is presented
9
10 here. In addition, laser ablation was not performed on a fix target area as it is commonly done,
11
12 but it was made with the laser beam scanning the target. On one hand this allows minimizing the
13
14 accumulation of laser pulses over damaged target areas, accumulation that varies both the
15
16 chemical composition and the energy thresholds for ablation of the target. On the other hand,
17
18 scanning helps keeping a reasonably similar local NP concentration of the liquid at the ablation
19
20 site, given that the site changes, and also that scanning favors the dissipation of the synthesized
21
22 NP cloud. Accordingly, the effect of scanning parameters was also scoped. Special attention was
23
24 paid to determine the iron species present in these NPs. Moreover, the influence of the use of
25
26 different solvents, from water to alcohols with increasing carbon to oxygen ratio, as well as the
27
28 presence in the solvent of stabilizing hydrophilic molecules were as well evaluated and
29
30 discussed. As a result, this work presents an unusually thorough characterization of as-
31
32 synthesized nZVI particles generated by LA-PLA, which brings to a well-supported discussion
33
34 about the optimum processing conditions.
35
36
37
38
39
40
41
42
43

44 **2. Experimental Section**

45 *2.1. Materials*

46
47 Commercial analytical-grade reagents were used. Bulk iron disks (thickness = 1.0 mm, purity =
48
49 99.5 %, diameter = 3 cm, body centered cubic α -Fe phase) were purchased from Goodfellow
50
51 Cambridge Ltd. Ethanol (EtOH), *1*-propanol (*1*-PrOH), 2-propanol (2-PROH), *1*-butanol (*n*-
52
53 BuOH), *tert*-butanol (*t*-BuOH) cyclohexanol (CH-OL), polyethylenglycol (PEG), poly(-vinyl)
54
55
56
57
58
59
60
61
62
63
64
65

pyrrolidone (PVP) K10, citric acid (CA) and polyethylenimine (PEI) were purchased from Sigma-Aldrich.

2.2. Lasers

Two different commercial high-power high-repetition pulsed-laser systems were used for nanoparticle generation: a pulsed multimode Q-Switched, diode pumped Nd:YAG fiber laser emitting in the infrared at 1050 nm (Easy Mark 20, Jeanologia: nominal power (P_m) = 20 W, pulse width (τ_p) = 4-200 ns and repetition rate (f) = 5-50 kHz); and a pulsed Q-Switched diode pumped Nd:YAG fiber laser emitting in the visible at 532 nm (Power Line, Rofin: P_m = 2 W, τ_p = 5-50 ns and f = 15-200 kHz). Both laser systems were equipped with a galvanometric scanning head controlled by a CAD-like software, which allowed precise control of the scan parameters of the laser beam over the target surface.

2.3. Nanoparticle synthetic procedure

Nanoparticle colloidal dispersions were synthesized by laser ablation of bulk iron disks placed in the bottom of a Pyrex glass cell, containing different solvents. In a typical synthesis experiment, the cell, containing the bulk iron disk and the solvent, was fitted on a lift platform and placed under the galvanometer head scan to match the disk surface with the focal distance required for each solvent (see Fig. 1). The focus distance for each solvent was calculated to keep the position of the target always slightly above the laser theoretical focus to avoid the breakdown of the liquid molecules produced by laser irradiation of the solvent. [16] A preliminary examination of the effect of the solvent column height (H) and irradiation time (t) on the nanoparticle productivity revealed that higher yields were obtained at H and t values around 5 mm (2 mL) and 502 s, respectively. These values, as well as the laser beam diameter at the target surface (30

μm), were fixed for the rest of the synthesis experiments summarized in this work. Other laser working parameters (laser wavelength, pulse repetition rate, pulse width, average laser pulse energy, fluence, pulse accumulation per spot, pulse overlap and scanning speed, see Fig. 1) and the nature of the solvent were systematically changed to explore their influence on the productivity and characteristics of the synthesized nanoparticles. Finally, several experiments were conducted to achieve in situ coating of the as-synthesized NPs with hydrophilic molecules. To do it, polyethyleneglycol and aqueous solutions (concentration 0.01 M) of water-soluble hydrophilic molecules (citric acid, poly(-vinyl) pyrrolidone K10 and polyethylenimine) were used as ablation media. After synthesis experiments, coated-NPs were separated via centrifugation and repeatedly washed with distilled water. The obtained solid was dispersed in distilled water and immediately dialyzed in 5 L for 24 h by using a 12 000-14 000 nominal molecular weight cutoff membrane (CelluSep F3, Membrane Filtration Products Inc.).

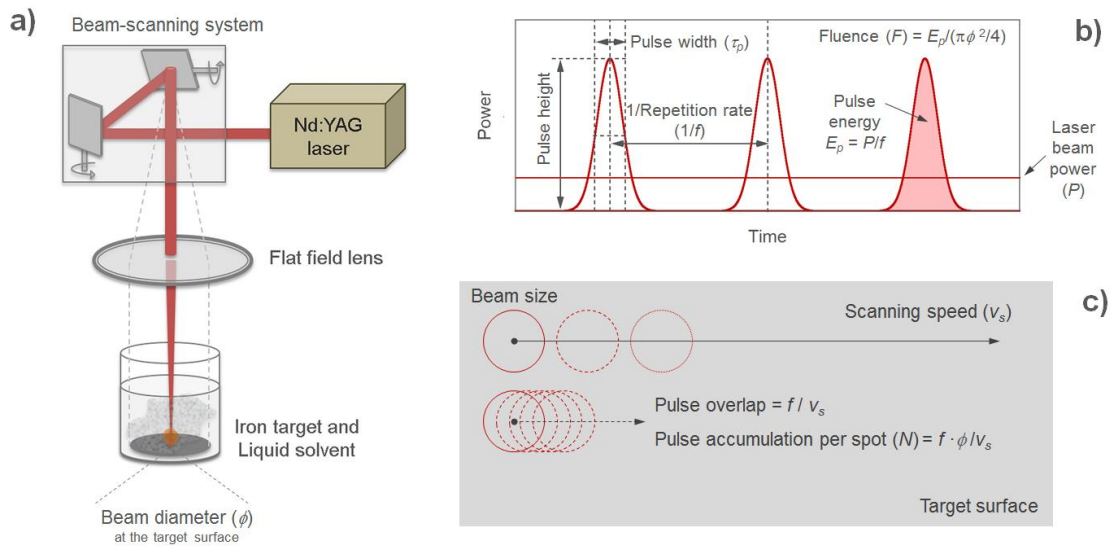


Fig. 1. a) Scheme of the experimental setup used in the synthesis of nZVI particles; b) laser pulse parameters; c) laser beam scanning parameters on target surface.

2.4. X-ray diffraction

The crystalline structure of the synthesized nZVI particles was studied by Grazing Incidence X-ray diffraction (GIXRD) analysis (Bruker D8 Advance Series 2 diffractometer with Cu K α radiation which is fitted with a grazing incidence attachment). GIXRD patterns were recorded between 10 and 65° (2 θ) with 0.050° step width and 5 s counting time. Specimens were prepared by dropping colloidal dispersions of these nanoparticles onto a silicon wafer and subsequent drying at room temperature.

2.5. Transmission Electron Microscopy

Particle size distribution was determined using a JEOL JEM1010 Transmission Electron Microscope (TEM) operated at 100 kV and a Philips CM200 at 200kV. For obtaining the size distribution of each NPs sample, around 2000 NPs were counted from the TEM images using the Image J software and the obtained particle size distribution was lognormally fitted with parameters μ (natural logarithm of the median diameter) and σ (standard deviation of the natural logarithm of the measured particle sizes). The mean particle diameter (D_{TEM}), the standard deviation ($Sd_{D_{TEM}}$) and the overall polydispersity index (PDI) of the size distribution were determined according to the following equations. [17]

$$D_{TEM} = \exp \left(\mu + \sigma^2 / 2 \right) \quad (1)$$

$$Sd_{D_{TEM}} = \exp \left(\mu + \sigma^2 / 2 \right) \sqrt{\exp \left(\sigma^2 \right) - 1} \quad (2)$$

$$PDI = \left(Sd_{D_{TEM}} / D_{TEM} \right)^2 \quad (3)$$

A detailed analysis of the nanostructure and composition of the synthesized nanoparticles were performed by using a F30 FEI Tecnai TEM microscope, operated at 300 kV, which was

equipped with a Gatan bottom-entry CCD camera 2K x 2K, Gatan “Tridiem” Energy Filter and an Energy-dispersive X-ray spectroscopy (EDS) detector. In addition, spherical aberration (C_s) corrected scanning transmission electron microscopy (STEM) observations using the high-angle annular dark-field (HAADF) technique, and electron energy loss spectroscopy (EELS) analysis of these nanoparticles were carried out in a Titan Low-base high-brightness source (XFEG), 60-300 kV operated at 300 kV. This microscope was equipped with a monochromator achieving an energy resolution of 0.18 eV, an EDS detector and a Gatan Tridiem Energy Filter for EELS measurements and CEOS corrector for the electron probe allowing a point resolution of 0.8 Å. EELS spectra were collected in the core-loss regions from 500 to 800 eV (O K and Fe $L_{2,3}$ edges) along line scans. Moreover, the analysis of the fine structure of the O and K near-edge electron energy loss spectrum (ELNES) was extracted from EELS spectra.

2.6. X-ray photoelectron spectroscopy and Laser Raman spectroscopy

X-ray photoelectron spectroscopy (XPS) was also used to determine the surface composition of these NPs. The spectra were measured with $MgK\alpha$ radiation in a CLAM-4 MCD spectrophotometer with a hemispherical analyzer system (Thermo VGScientific, 9-channeltron system) in an ultra-high vacuum chamber (3×10^{-10} mbar of pressure). The effective depth of measurement, as a function of the experimental conditions used in this analysis, is about 4 nm. In addition, a confocal micro laser Raman microscope (LRS), model Witec ALPHA 300RA, was used to determine the iron oxide and/o iron-carbon alloy phases present in the as-synthesized nanoparticles. Raman spectra were excited by the 532 nm line of a Nd:YAG laser with an output power of 1 mW and collected in a backscattering geometry with spectral resolution of 0.02 cm^{-1} . These spectra were analyzed by using the Project Four 4.1 software.

2.7. Magnetic measurements

The magnetic properties of the synthesized NPs were studied with a superconducting quantum interference device (SQUID) magnetometer, namely the MPMS-XL from Quantum Design. Magnetization-vs.-field, $M(H)$, measurements were performed at 300 K with dc fields ranging from 0 to 5 T to obtain first magnetization curves and hysteresis loops. To this end, the synthesized colloidal nanoparticles were previously dried at room temperature. After magnetic measurements, the iron content of these dried NPs was determined using an Inductively Coupled Plasma-Optical Emission Spectrometer (ICP-OES Spectroblue from AMETEK) calibrated with single-element Fe standards. For this purpose, NPs synthesized in DW were digested in aqua regia at 90°C and diluted in distilled water up to a volume of 25 mL. NPs synthesized in EtOH were digested in a mixture of HNO₃ (68%) and HF (48%) inside a PARR acid digestion vessel at 125°C for 4 hours. The obtained solution was diluted in distilled water up to a volume of 50 mL. Magnetization values were calculated directly using the iron mass ($\text{emu} \cdot \text{g}_{\text{Fe}}^{-1}$). Diamagnetic contributions coming from the sample holder were subtracted from the measured data.

2.8. Ablation rate and colloidal properties

Evaluation of the iron concentration ($\text{mg}_{\text{Fe}} \cdot \text{mL}^{-1}$) in the nanoparticle colloidal dispersions (except for magnetic measurements) was performed via Total Reflection X-ray Fluorescence (TXRF) by using a TXRF 8030c, FEI spectrometer. From these results the ablation rate ($\text{mg}_{\text{Fe}} \cdot \text{mL}^{-1} \cdot \text{h}^{-1}$) was calculated. Moreover, dry weight of the NPs samples ($\text{mg}_{\text{NP}} \cdot \text{mL}^{-1}$) were performed by measuring, with a high precision microbalance, the weight of the residue obtained after drying at room temperature 1 mL of the as-synthesized nanoparticle colloidal dispersions. These results allowed obtaining a measure of the additional amount of material produced during the ablation

process, which is present together with the as synthesized nanoparticles, such as carbon (in the form of amorphous carbon or graphite) or oxygen (oxygen (in the form of iron oxide). The hydrodynamic size (DH), overall DH polydispersity index (PDI_H) and zeta potential of these dispersions was measured by using a Malvern Zetasizer Nano-ZS (Malvern Instruments, Worcestershire, U.K.). These measurements were performed at the same nanoparticle concentration as the synthesized NPs samples. To do this, an aliquot of the synthesized NPs colloidal dispersions was taken immediately after the synthesis of each sample. Subsequently, this aliquot was placed into the cuvette and measured immediately without dilution. Each measurement was repeated at least three times and the mean values were calculated. DH was reported as the number weighted average diameter. Zeta potential of the as-synthesized samples was measured as a function of pH at 25 °C. The pH values of the dispersions were measured by a combination electrode and adjusted with dropwise addition of 0.1M NaOH or HCl solutions.

3. Results and Discussion

3.1. NPs synthesized in DW and EtOH with initial laser parameters

Direct synthesis of colloidal dispersions of nZVI particles were firstly attempted via laser ablation of bulk α -Fe disks submerged in distilled water (DW) or ethanol (EtOH) using the experimental setup schematized in Fig. 1 and experimental conditions that allowed a sufficient production of particles for further analysis: laser wavelength $\lambda = 1050$ nm, pulse repetition rate $f = 25$ kHz (or kpulses/s), pulse width $\tau_p = 50$ ns, average laser pulse energy $E_p = 0.137$ mJ, fluence $F = 19.35$ J·cm⁻², pulse accumulation per spot $N = 6$ (pulse overlap = 200 pulses·mm⁻¹), and scanning speed (v_s) = 125 mm·s⁻¹. DW and EtOH were chosen because they are polar solvents and miscible in any proportion but exhibit different chemical composition and physical

properties (see SI, Table S1). The Fe concentration in the as synthesized dispersions, estimated by TXRF, was around 57 and 95 mg·L⁻¹ for EtOH and DW, respectively (with a dried nanoparticle weight of 68 and 228 mg_{NP}·mL⁻¹, respectively), yielding to an ablation rate of 408 mg·L⁻¹·h⁻¹ and 681 mg·L⁻¹·h⁻¹, respectively.

3.1.1. Size, shape and structure of NPs

Fig. 2 displays TEM results of the nanoparticles synthesized using DW (DW-NPs, Sample 1) and EtOH (EtOH-NPs, Sample 2) as solvent. TEM (Fig. 2a) and STEM (Fig. 2b and Fig. S1c in SI) images of the former revealed the existence of roughly spherical NPs (4-50 nm in size) embedded inside a matrix, while TEM (Fig. 2d) and STEM (Fig. 2g) images of the later showed well-isolated and spherical NPs (4-117 nm in size). Both kind of NPs showed lognormal size distributions (Fig. 2c), with mean particle size (D_{TEM}) of 9.4 nm and 13.5 nm, respectively, and standard deviation ($Sd_{D_{TEM}}$) of and 4.8 nm (polydispersity index, $PDI \sim 0.26$) and 9.5 nm ($PDI \sim 0.50$), respectively.

HRSTEM images (zooms in Fig. 2b and Fig. S1d in SI) of DW-NPs revealed crystal lattice fringes that were not present in the surrounding amorphous matrix. Fast Fourier Transform (FFT) patterns of these images resulted in interplanar distances corresponding to a cubic inverse spinel structure, either magnetite (Fe₃O₄) [18] or maghemite (γ-Fe₂O₃). [19] According to these results, nZVI particles were not directly obtained via laser nanosecond laser ablation of massive iron targets by using pure DW as solvent. The GIXRD pattern of these NPs confirmed this finding (see Figure S1a in SI).

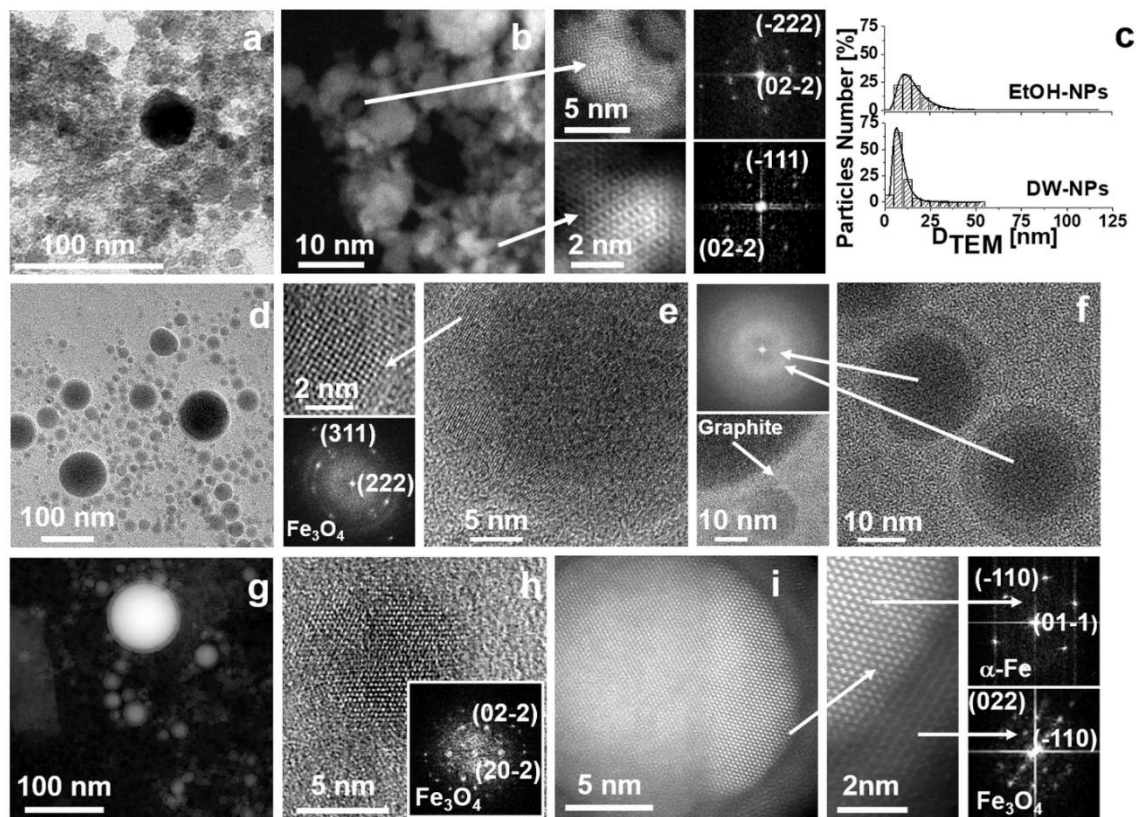


Fig. 2. Size, shape and structure characterization of synthesized NPs: a) low magnification TEM image of DW-NPs; b) low magnification Cs-corrected STEM image and Cs-corrected HRSTEM (zooms of (b)) image of crystalline DW-NPs (bright areas) inside an amorphous matrix, together with obtained FFTs; c) size distribution histograms of as synthesized DW-NPs and EtOH-NPs; d) low magnification TEM of synthesized core-shell EtOH-NPs; e) HRTEM images of the shell of EtOH-NPs showing lattice fringes, together with obtained FFTs; f) HRTEM images of EtOH-NPs showing amorphous cores with FFTs (upper left image) and detail of a graphitic outer layer formed after plasma cleaning of EtOH-NPs (lower left image); g) low magnification STEM of synthesized core-shell EtOH-NPs; h) HRTEM image of a small NPs synthesized under EtOH; and i) Cs-corrected HRSTEM image of an EtOH-NP showing lattice fringes inside the core and the shell, together with obtained FFTs.

In EtOH-NPs, three distinct structures were found. Like in DW-NPs, EtOH-NPs smaller than 8 nm were monocrystalline, showing a FFT pattern with interplanar distances related to cubic γ - $\text{Fe}_2\text{O}_3/\text{Fe}_3\text{O}_4$ phases (Fig. 2h). However, EtOH-NPs higher than 8 nm showed a well-constructed core-shell structure (Fig. 2f), in good accordance with the results published by Amendola *et al.* [12a] and Sukhov *et al.* [14a]. HRTEM (Fig. 2e) and HRSTEM (Fig. 2i) showed that this shell

was 3-5 nm thick and well crystallized, showing planes of cubic γ -Fe₂O₃/Fe₃O₄ phases, like in small NPs. A certain amount of amorphous carbon was present on the surface, evidenced by the appearance of a layer of crystalline graphitic carbon after they were subjected to a plasma cleaning process (lower left image in Fig. 2f). Moreover, most of these core-shell NPs showed an amorphous core, presumably composed of iron (upper left image in Fig. 2f). Only through an exhaustive HRSTEM analysis it was possible to detect a small fraction of larger NPs (> 30 nm) that presented a certain degree of crystalline order inside the core, showing interplanar distances of a BCC α -Fe phase (Fig. 2i). [20] The predominantly amorphous nature of EtOH-NPs cores was also confirmed by GIXRD analysis (see Fig. S1b in SI).

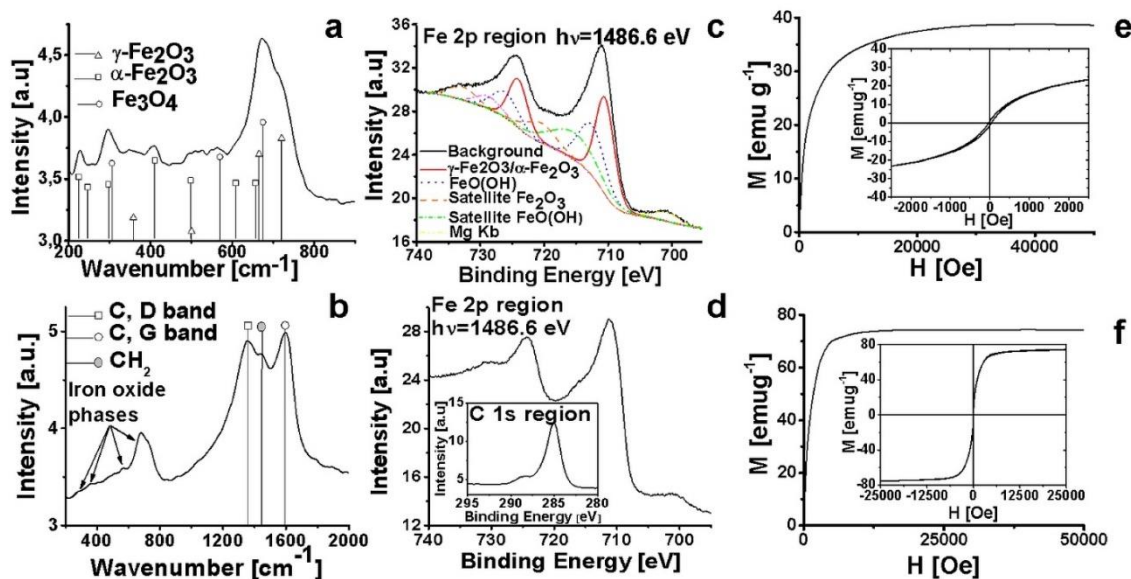


Fig. 3. Spectroscopic and magnetic characterization of as-synthesized DW-NPs (upper) and EtOH-NPs (lower): LRS spectra of (a) DW-NPs and (b) EtOH-NPs; Fe2p region of the XPS spectra recorded for (c) DW-NPs and (d) EtOH-NPs (showing C1s spectrum in the inset); first magnetization vs. magnetic field (M-H) curves and detail of hysteresis loops (insets) recorded for DW-NPs (e) and EtOH-NPs (f).

3.1.2. Chemical composition of NPs

Especially due to the presence of amorphous material both in DW-NPs and in EtOH-NPs, different spectroscopic studies were performed to complement structural characterization. LRS analysis of DW-NPs (Fig. 3a) and EtOH-NPs (Fig. 3b) revealed the presence of peaks corresponding to γ -Fe₂O₃/Fe₃O₄ and, also, FeO phases (see Fig. S1bis at SI for a detailed LRS analysis), [21] in good accordance with data obtained from TEM, STEM and GIXRD. Moreover, in DW-NPs four peaks were detected which correspond to a α -Fe₂O₃ or a FeO(OH) phase. [21b] Because HRTEM analysis did not detect this phase inside the NPs, this suggest that a α -Fe₂O₃ and/or a FeO(OH) phase was the main component of the poorly crystalline matrix. Additionally, in EtOH-NPs two intense peaks were observed that correspond respectively to the D band of amorphous carbon materials (1360 cm⁻¹) and the G band of crystalline graphitic carbon (1595 cm⁻¹), [22] and a smaller peak (1450 cm⁻¹), which is related to -CH₂ groups from EtOH molecules physisorbed on the nanoparticles surface. [23] Thus, the existence of iron carbide phases could be discarded due to the absence in this spectrum of an intense band at 2700 cm⁻¹ (2D band). [24] Moreover, the intensity of D and G bands was similar, indicating that the carbonaceous material is mostly amorphous carbon. [25] These data, together with HRTEM results, suggested that nanoparticle carbonaceous contamination occurred without carburization. Thus, the amorphous carbon could appear as a solid solution inside the iron cores, which could explain the poor crystalline order. [26]

Local compositional information was obtained from EDS and EELS analysis. Fig. 4a displays a STEM image of a large DW-NP (~ 50 nm) with three labeled areas: M (amorphous matrix), E (DW-NP surface) and C (NP center). Relative atomic concentration profiles of Fe and O

obtained from EELS (insets in Fig. 4b and 4c) and EDS spectra (Fig. S1f in SI) yielded Fe/O atomic ratios from 0.60 to 0.66 in the matrix (close to those reported for Fe_2O_3 [27]), from 0.70 to 0.78 in the DW-NP surface (related to those reported for Fe_2O_3 and Fe_3O_4 [27]) and close to 0.95 in the center, suggesting the presence in these large NPs of a wüstite core. [27] O K-edge ELNES spectra allowed further information of present iron oxide phases through the analysis of four possible distinct positions around 530 eV, 540 eV, 545 - 550 eV and 560 - 566 eV (labeled as A, B, C and D, respectively). The spectrum at M (Fig. 4b) is characteristic of $\alpha\text{-Fe}_2\text{O}_3$ (absence of peak C) [27] confirming that the matrix was mainly hematite. ELNES spectrum at E (Fig. 4c) is in good accordance with those reported for the shell of an oxide shell-iron core NPs (presence of the four peaks), where the shell consisted of $\gamma\text{-Fe}_2\text{O}_3$ or a solid solution between $\gamma\text{-Fe}_2\text{O}_3$ and Fe_3O_4 . [26] Also, ELNES spectrum (Fig. 4c) recorded at C is compatible with the presence of a wüstite core (decrease of peaks A and C). [27] These results confirm the fact that nZVI particles were not directly obtained using pure DW as solvent.

Fig. 4d and 4g show STEM images of representative iron-iron oxide core-shell EtOH-NPs. In particular, Fig. 4d presents two labeled areas: A (outer edge of the oxide shell) and B (shell-core interface). The ELNES spectrum at A was like those reported for a $\gamma\text{-Fe}_2\text{O}_3/\text{Fe}_3\text{O}_4$ phase. [28] On the contrary, the absence of the C peak in the ELNES spectrum at B, together with the reduction in the depression between the peaks A and B, indicated the majority presence of a FeO phase. [27] This variation in the shell composition was confirmed via quantification of the Fe/O atomic ratio by EELS along the spectrum profiles in Fig. 4d and 4g. Thus, an increase in the Fe/O atomic ratios from 0.35-0.50 (relating to $\gamma\text{-Fe}_2\text{O}_3/\text{Fe}_3\text{O}_4$ phase partially transformed to $\text{FeO}(\text{OH})$) to 0.9 (corresponding to FeO) were detected as moving from the outer edge of the oxide shell to the shell/core interface (Fig. 4f, 4h and 4i). Eventually, Fe/O ratios atomic higher than 8 were

calculated inside the core (Fig. 4i), demonstrating that it consists mainly of iron and confirming the direct formation of nZVI particles in EtOH. Note that a portion of upper shell is always analyzed with the core, leading to lower Fe/O ratios than those really present in the core.

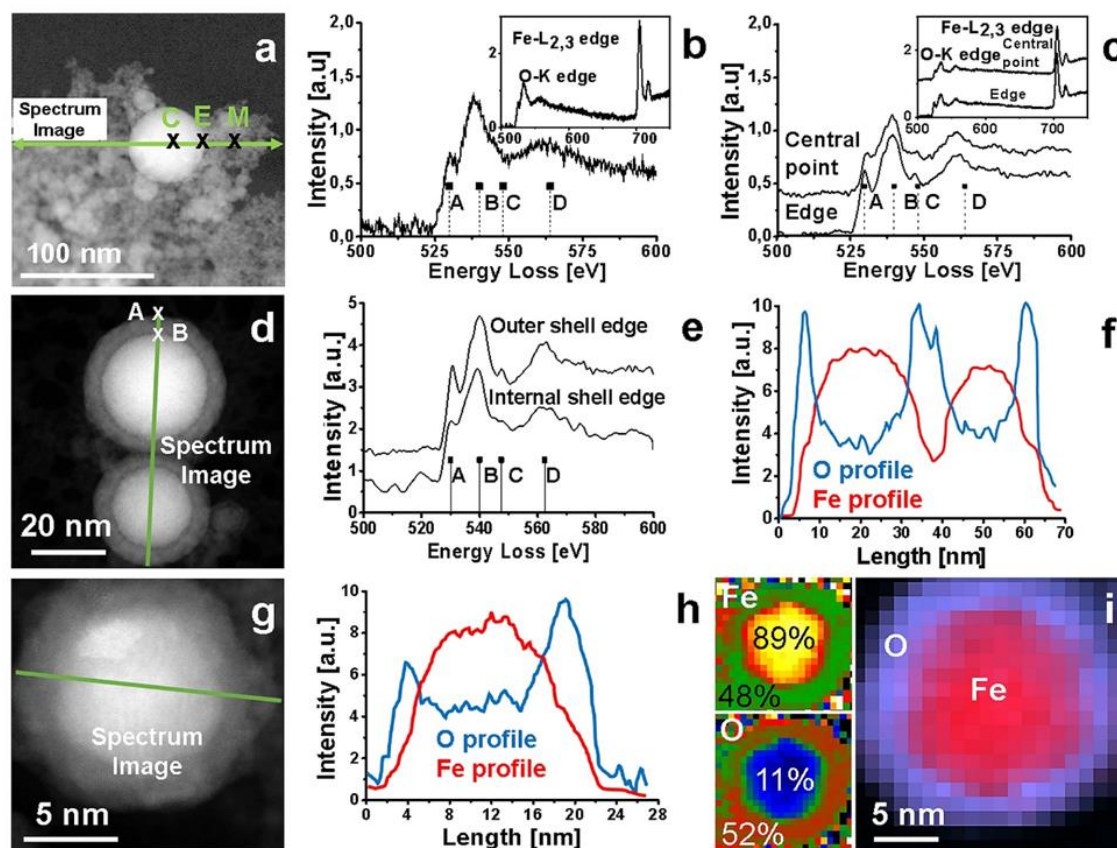


Fig. 4. EELS analysis of the as synthesized DW-NPs (a-c) and EtOH-NPs (d-i): a) STEM image of DW-NPs, where an EELS line scan was conducted; b) O K-edge ELNES spectrum recorded in the area marked as M in figure a (inset: EELS spectrum recorded in this area); c) O K-edge ELNES spectra recorded in the areas marked as C and E in figure a (inset: EELS spectra recorded in these areas); d) STEM image of two EtOH-NPs, where an EELS profile was conducted; e) O K-edge ELNES spectra recorded in the areas marked as A and B in figure d; f) Fe and O concentration profiles obtained from the EELS spectra recorded along the line scan in figure d; g) STEM image where a EELS profile was conducted; h) Fe and O concentration profiles obtained from the EELS spectra recorded along the line scan in figure g; i) Fe and O concentration mapping obtained from the EELS spectra recorded in figure g.

EELS results agreed with those obtained from XPS. The analysis of Fe2p region of the spectra recorded for DW-NPs (Fig. 3c) and EtOH-NPs (Fig. 3d) (see Fig. S1bis at SI for a detailed XPS analysis) showed the presence of peaks characteristic of the Fe³⁺ cations of Fe₂O₃ [29] and the

iron (III) hydroxide ($\text{Fe}(\text{OH})_3$). [29] The fact that no additional peaks related to the presence of Fe^{2+} or Fe were detected in EtOH-NPs was attributed to the analysis depth of XPS. Moreover, C1s spectrum of EtOH-NPs (inset in Fig. 3d) showed the presence of C-C bonding carbon bonds, C-O bonds from physisorbed EtOH molecules and $\text{C}\equiv\text{O}$ from physisorbed CO species, [25, 30] while iron carbide phases were not detected.

3.1.3. Colloidal properties of the obtained dispersions

Characterization of the colloidal properties were conducted at the original Fe and NPs concentrations obtained for DW-NPS and EtOH-NPs samples (see table 2), without dilution. In the case of DW, a brownish dispersion was obtained by laser irradiation, where DW-NPs showed DH and PDI_H values around 166 nm and 0.25 respectively. Unfortunately, this dispersion was rapidly destabilized, leading to the formation of large aggregates that precipitated in a few minutes. The zeta potentials of these NPs showed an isoelectric point (IEP) around 6.5, within the range of values reported for the iron oxide and oxy-hydroxide species detected in these NPs ($\alpha\text{-Fe}_2\text{O}_3$, IEP from 5.2 to 8.6; $\gamma\text{-Fe}_2\text{O}_3$, $IEP = 6.7$; Fe_3O_4 , $IEP = 6.5$; $\text{FeO}(\text{OH})$, IEP from 6.7 to 7.4). [31] In contrast, laser ablation under EtOH yielded to a slightly dark dispersion, which remained stable and without visible NPs sedimentation for several weeks. EtOH-NPs showed DH and PDI_H values around 207 nm and 0.42 respectively. They could be concentrated by centrifugation at 8000 rpm and transferred to distilled water, yielding to water colloidal dispersions of nZVI particles, which displayed larger DH and PDI_H values around 544 nm and 0.44, respectively. These dispersions showed an isoelectric point around 4.1, remaining stable in DW for several months at room temperature and neutral (7.0) and physiological pH (7.4). It is important to note that the zeta potential for EtOH-NPs transferred to DW is lower than those reported in the bibliography for nZVI nanoparticles ($IEP \sim 8.3$). [32] This shift could be

attributable to the partial presence on their surface of amorphous carbon species (*IEP* from 2.2 to 7.9) [33] and/or graphite (*IEP* from 3 to 4.5), [34] since further oxidation of the iron core of EtOH-NPs after being transferred to DW may be considered to have limited influence on the oxidized surface characteristics.

3.1.4. Magnetic characterization

First magnetization vs. magnetic field (*M-H*) curves and hysteresis loops were recorded at room temperature for dried DW-NPs (Fig. 3e) and EtOH-NPs (Fig. 3f). The later ICP-OES analysis of the analyzed samples gave iron weight percentages of 48.3% and 52.6%, respectively. Since both samples contained several iron compounds, magnetization was calculated directly using the iron mass ($\text{emu} \cdot \text{g}_{\text{Fe}}^{-1}$). The *M-H* curve of DW-NPs reveals a ferromagnetic behavior together with a quasi-linear trend. Such trend becomes evident at $H > 3 \cdot 10^4$ Oe, where the ferromagnetic magnetization gets saturated with a saturation magnetization value (M_S) of $38.70 \text{ emu} \cdot \text{g}_{\text{Fe}}^{-1}$. This value is appreciably lower than those reported for the ferrimagnets $\gamma\text{-Fe}_2\text{O}_3$ ($\sim 80 \text{ emu} \cdot \text{g}^{-1} \equiv 114 \text{ emu} \cdot \text{g}_{\text{Fe}}^{-1}$) and Fe_3O_4 ($\sim 94 \text{ emu} \cdot \text{g}^{-1} \equiv 131 \text{ emu} \cdot \text{g}_{\text{Fe}}^{-1}$) [35], but is consistent with the presence of an amorphous matrix of $\alpha\text{-Fe}_2\text{O}_3$ surrounding the $\gamma\text{-Fe}_2\text{O}_3/\text{Fe}_3\text{O}_4$ NPs. Hematite is an antiferromagnet that presents only a weak ferromagnetism ($M_S \sim 0.4 \text{ emu} \cdot \text{g}^{-1} \equiv 0.6 \text{ emu} \cdot \text{g}_{\text{Fe}}^{-1}$) due to spin canting at room temperature. This phase then lowers the M_S value of the sample as a whole. The observed linear trend can be partially ascribed to the antiferromagnetism of hematite, but mainly to surface effects leading to a magnetically dead layer, typical of ferrimagnetic NPs. [36] The *M-H* curve of EtOH-NPs presents as well ferromagnetic and linear contributions, although the ferromagnetic magnetization saturates already by 10^4 Oe, with $M_S = 74.34 \text{ emu} \cdot \text{g}_{\text{Fe}}^{-1}$. Even if most of these NPs present a Fe core and a $\gamma\text{-Fe}_2\text{O}_3/\text{Fe}_3\text{O}_4$ shell, their M_S value is far

from the values reported for bulk α -Fe ($220 \text{ emu}\cdot\text{g}^{-1}$), [35] amorphous Fe ($\sim 130 \text{ emu}\cdot\text{g}^{-1}$), [37] and nearer but still lower than those reported for γ -Fe₂O₃ and Fe₃O₄. This reduction in M_s is typical of core-shell NPs and can be attributed to the presence of magnetically dead layers both at the core and shell surfaces, [38] either due to disorder or/and stoichiometric variations giving rise to non-ferromagnetic iron compounds, (e.g. FeO(OH) or FeO, as shown above). Nonetheless, these NPs show a good M_s value among similar NPs fabricated by LA-PLA. [30, 39]

The hysteresis loops of both DW-NPs and EtOH-NPs have a sigmoidal shape, typical of superparamagnetic NPs. While the latter displays no hysteresis, the former shows a very low coercive value ($\sim 34 \text{ Oe}$). As a rough estimation, the critical diameters separating superparamagnetic and single domain ferromagnetic behaviors are 30 nm and 25 nm for γ -Fe₂O₃ and Fe₃O₄, respectively. [40] Accordingly, the non-zero coercive field of DW-NPs can be attributed to the presence of a small fraction of NPs with 25 to 40 nm in size, which is thermally blocked. On the contrary, EtOH-NPs show a complete superparamagnetic behavior.

3.2. Influence of laser and scanning parameters in EtOH-NPs

In the pursuit of optimal conditions for production of reproducible nZVI particles, the influence of the pulse width, wavelength, repetition rate, fluence, pulse number per spot and target scanning speed was analyzed. Table 1 and Fig. 5 summarize the effect of these variations on the final properties of the as-synthesized nZVI particles. The study was performed irradiating the iron target under EtOH since, according to the above results, nZVI NPs are directly produced with this solvent. When not mentioned, laser working parameters reported at the beginning of section 3.1 for EtOH-NPs were used by default.

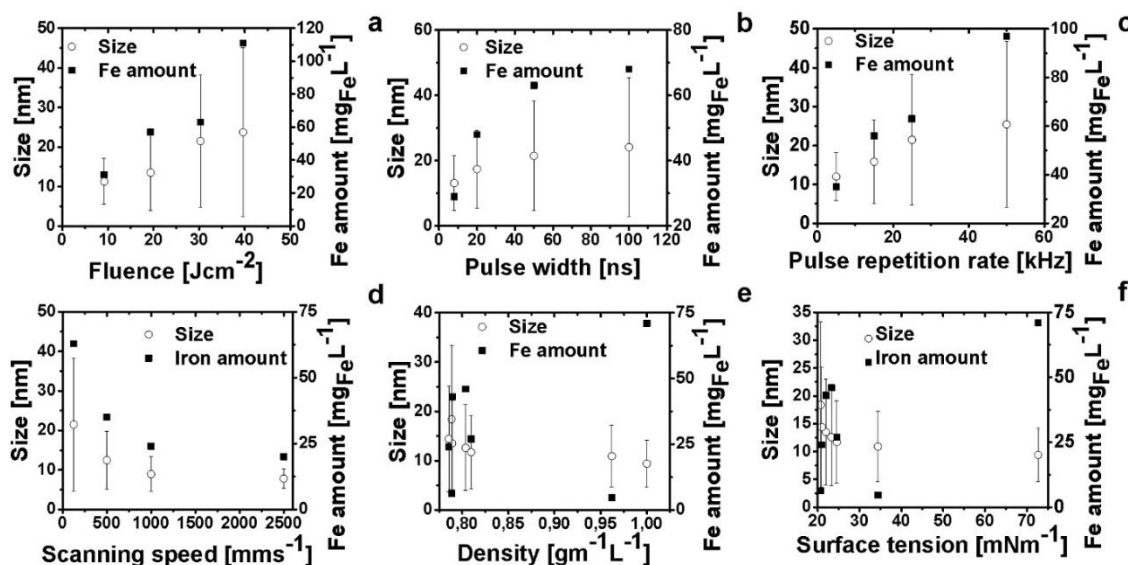


Fig. 5. Effect of laser processing variables on NP size and productivity: a) fluence (Samples 2, 4-6); b) pulse width (Samples 5, 7-9); c) pulse repetition rate (Samples 5, 10-12); d) scanning speed (Samples 5, 13-15). Effect of physical properties [density (e) and surface tension (f)] of the different solvents used as ablation media (Samples 2, 16-20).

3.2.1. Laser wavelength

For studying the role of the laser wavelength, new NPs were synthesized (Sample 3) using the visible pulsed-laser system described in the experimental section. TEM images (see SI Fig. S2) revealed the presence of spherical core-shell nanoparticles (3 to 500 nm) embedded inside a matrix, similarly to DW-NPs. But unlike DW-NPs, SAED (inset in SI Fig. S2c) patterns

recorded for this matrix showed the typical diffraction rings for amorphous carbon. The size of the NPs was lognormally distributed with D_{TEM} (12.4 nm), SdD_{TEM} (9.2 nm) and PDI (0.54) values, near to EtOH-NPs obtained by using the infrared laser. SAED patterns recorded for these NPs (SI Fig. S2d left) showed well crystallized iron oxide phases (cubic γ -Fe₂O₃/Fe₃O₄ and a trigonal α -Fe₂O₃), as well as an orthorhombic iron carbide phase, type cementite (Fe₃C). [41] EDS analysis in the shell revealed Fe/O ratios around 0.70 (SI Fig. S2e top), in good accordance with the existence of an external layer of a Fe₂O₃-Fe₃O₄ mixture. The high Fe contents detected by EDS inside the NPs core (SI Fig. S2e down) could suggest that it is composed of Fe and Fe₃C. This is conversely to EtOH-NPs synthesized with the infrared laser, where iron carbide phases have not been detected. The existence of this iron carbide phase, together with the presence of the amorphous carbonaceous matrix, suggested a strong interaction between the visible laser beam and the EtOH during the ablation process, yielding to a significant carburization and carbonaceous contamination of the synthesized NPs, which resulted in non-isolated NPs.

3.2.2. Average laser pulse energy

The influence of E_p was secondly studied by increasing it from 0.065 mJ ($F = 9.17 \text{ J}\cdot\text{cm}^{-2}$, Sample 4) to 0.280 mJ ($F = 39.61 \text{ J}\cdot\text{cm}^{-2}$, Sample 6) through variation of the laser beam power (P) (see Table 1). Note that E_p is calculated as P/f . TXRF analysis showed that this increment yielded to an increase in the Fe concentration in the obtained dispersions from 31 to 111 mg_{Fe}·mL⁻¹, resulting in a boost of ablation rate from 222 to 796 mg_{Fe}·L⁻¹·h⁻¹ (Fig. 5a). However, a strong surface contamination with carbon compounds was observed in NPs synthesized by using high pulse energies. TEM images (SI Fig. S3a and S3d) showed that core-shell nanoparticles were obtained in all cases. Statistical analysis revealed that these NPs exhibited a

lognormal size distribution, and that the increase in E_p yielded to an increase in the D_{TEM} from 11.3 ± 5.9 nm to 23.7 ± 21.3 nm (Fig. 5a and SI Fig. S4), enlarging also the PDI value from 0.27 to 0.81 (Table 1). HRTEM analysis revealed a NP structure like those reported for nominal EtOH-NPs (Sample 2), with a progressive increase in the iron core crystallinity as E_p got larger. Thus, nZVI particles obtained at lower E_p values showed mainly a metallic glass core structure (SI Fig. S3b), whereas more numerous NPs synthesized by using higher E_p values presented cores with some degree of crystalline order, with lattice fringes corresponding to a cubic α -Fe phase (SI Fig. S3e). This fact might be related to the increase of the particle size. Moreover, LRS spectra recorded for these NPs (SI Fig. S3c) indicated a progressive increase in the intensity of the D and G bands of carbon, as well a strong decrease in the peak assigned to γ -Fe₂O₃/Fe₃O₄. This matched well with a progressive thickening of the coating of the NPs by a layer of amorphous carbon.

3.2.3. Pulse width

The role of the pulse width was found to be like that of E_p . It was evaluated by changing it from 8 ns (Sample 7) to 100 ns (Sample 9) with constant P (5.35 W) and f (Table 1). Then, the increase of τ_p implies a decrease in pulse height. An increase in the Fe concentration from 29 to 68 mg_{Fe}·L⁻¹ (and in the ablation rate from 208 to 488 mg_{Fe}·L⁻¹·h⁻¹) was detected, just as it was observed increasing E_p values. TEM analysis (see Fig. 5b and SI Fig. S5) revealed that this increase in τ_p values yielded to a progressive enlargement of the D_{TEM} and PDI values from 13.1 ± 8.4 nm to 24.1 ± 21.34 nm and from 0.41 to 0.78, respectively (Table 1). In addition, a progressive thickening of the coating of the NPs surface with amorphous carbon and/or

crystalline graphite (SI Fig. S5f), as well as an increase in the crystalline order of the NPs core, were detected as τ_p values got longer (SI Fig. S5g and S5h).

3.2.4. Pulse accumulation per spot

The influence of the applied N value was first analyzed by modifying the pulse repetition rate from 5 kHz (Sample 10, $N \approx 1$) to 50 kHz (Sample 12, $N \approx 12$) with constant P (5.35 W) and v_s (Table 1). In this case, similar results to that of the variation of E_p were obtained. TEM analysis (SI Fig. S6 left) indicated that the variation of N from 1 to 12 resulted in a lognormally distributed NP population, which showed an increase in D_{TEM} and PDI values from 12.1 ± 6.2 nm to 25.4 ± 21.3 nm (Fig. 5c) and from 0.27 to 0.70, respectively, displaying the same iron core/iron-oxide shell structure (zooms 1 and 2 in SI Fig. S6b and S6d). Moreover, an increase in the Fe concentration in the obtained dispersions from $35 \text{ mg}_{\text{Fe}} \cdot \text{mL}^{-1}$ (ablation rate of $251 \text{ mg}_{\text{Fe}} \cdot \text{mL}^{-1} \cdot \text{h}^{-1}$) to $97 \text{ mg}_{\text{Fe}} \cdot \text{mL}^{-1}$ (ablation rate of $696 \text{ mg}_{\text{Fe}} \cdot \text{mL}^{-1} \cdot \text{h}^{-1}$) was also detected. It is important to note that the considered f interval produced an increase in the N value from 1 to 12 as well as a reduction in E_p from 1.07 mJ to 0.11 mJ (F from $30.3 \text{ J} \cdot \text{cm}^{-2}$ to $15.1 \text{ J} \cdot \text{cm}^{-2}$). In view of the results described above for E_p , a decrease in D_{TEM} would be expected. However, the observed increase in D_{TEM} , despite the decrease in E_p suggested that N plays a key factor to control the particle size and nanoparticle productivity during the generation of NPs by LA-PLA.

This finding was confirmed by the experiments conducted changing N via modification of the scanning speed from $125 \text{ mm} \cdot \text{s}^{-1}$ (Sample 5, $N = 6$) to $2000 \text{ mm} \cdot \text{s}^{-1}$ (Sample 15, $N \approx 1$) without variation of P (5.35 W) and f (Table 1). TEM analysis (SI Fig. S6 right) revealed that the reduction of N from 6 to 1 produced a decrease in D_{TEM} from 21.5 ± 16.9 nm to 7.8 ± 2.5 nm (Fig. 5d), but without the loss of the iron core/iron-oxide shell structure (SI Fig. S6i and S6j)

observed in Sample 2 for such small EtOH-NPs. This resulted, also, in a decrease of *PDI* from 0.61 to 0.10. These NPs could be transferred to DW, yielding to stable water colloidal dispersions of nZVI particles with particle size distributions showing *DH* and *PDI_H* values around 215 nm and 0.32, respectively. These values are in the limit of those allowed for use in medicine or environmental remediation, and were obtained without the necessity to introduce surfactant or capping agents to control the particle size. Unfortunately, this increase in the v_s values resulted in a decrease in the iron concentration of the colloidal dispersion from 63 mg_{Fe}·mL⁻¹ (ablation rate ~ 452 mg_{Fe}·mL⁻¹·h⁻¹) to 20 mg_{Fe}·mL⁻¹ (ablation rate ~ 143 mg_{Fe}·mL⁻¹·h⁻¹). Therefore, the generation of nZVI particles by laser ablation at high v_s values would have to be accomplished by using high E_p values to balance the reduction in polydispersity with enough production of NPs.

3.3. NPs synthesized in other alcohols

In section 3.1 it was demonstrated that the solvent plays an important role in the generation of nZVI particles by liquid-assisted pulsed laser ablation. Considering that core-shell nZVI particles were obtained only by using EtOH as solvent, other alcohols with different (short and medium) hydrocarbon chain lengths and/or configurations (*1*-PROH, *2*-PROH, *n*-BuOH, *t*-BuOH and CH-OL), which show different physicochemical properties (**Table 2** and SI Table S2), were evaluated as ablation environments, using the laser working parameters reported at the beginning of section 3.1 for EtOH-NPs. Thus, stable slightly grayish dispersions were obtained in the case of the experiments conducted under EtOH, *1*-PROH (Sample 16) and *2*-PROH (Sample 17), whereas unstable and black dispersions were obtained by using *n*-BuOH (Sample 18), *t*-BuOH (Sample 19) and CH-OL (Sample 20). Moreover, the dried NP weight was found to be appreciably higher in unstable dispersions than in stable ones, ranging from 68 mg_{NP}·L⁻¹ (EtOH)

1
2
3
4 to 286 mg_{NP}·L⁻¹ (CH-OL). However, TXRF analysis revealed that this increase in the dried NP
5
6 weight coincided with a strong decrease in the Fe concentration in the colloidal dispersion. It was
7
8 especially low for non-linear chain alcohols and ranged from 43 mg_{Fe}·L⁻¹ (EtOH) to 4.6 mg_{Fe}·L⁻¹
9
10 (CH-OL) (Table 2).
11
12
13
14

15 As reported for EtOH-NPs, roughly spherical NPs were obtained in these experiments, regardless
16
17 of the alcohol used (SI Fig. S7). These NPs showed, in all cases, well-constructed core-shell
18
19 structures, with crystalline iron-oxide shells and crystalline or amorphous iron cores. Moreover,
20
21 they displayed lognormal particle size distributions, with sizes varying from 18.4 ± 14.9 nm
22
23 (*PDI* = 0.66) to 10.9 ± 6.3 nm (*PDI* = 0.33) for *t*-BuOH and CH-OL, respectively (SI Fig. S8).
24
25 Neither of these magnitudes correlates with the number of carbons of the solvents. However, the
26
27 reported decrease coincided with an increase in the density (δ) and surface tension (σ) of these
28
29 alcohols, suggesting a significant role of these physical parameters (Fig. 5e and 5f). This
30
31 decrease is linear for alcohols of linear chains. On the other hand, HRTEM images (SI Fig. S7a,
32
33 S7c, S7f, S7h and S7i) showed that the use of alcohols with increasing number of carbons
34
35 yielded to the embedding of the iron core/iron-oxide shell NPs inside a matrix. Plasma cleaning
36
37 of the microscope grids of these samples yielded to the complete removal of this matrix and the
38
39 coating of all NPs with an outer layer of crystalline graphite, suggesting clearly that this matrix
40
41 consists in amorphous carbon. This coating was more abundant in the case of *n*-BuOH, *t*-BuOH
42
43 and CH-OL, where some NPs display an outer rim of graphite (SI Fig. S7f and S7h). Moreover,
44
45 in the case of samples synthesized under CH-OL, small nanoparticles around 1-2 nm in size were
46
47 also observed. SAED analysis of these NPs (SI Fig. S7i) revealed the characteristic rings of the
48
49 amorphous carbon. The presence of these carbonaceous species as a matrix could explain the
50
51 higher dried NP weight of these samples, as well as their colloidal instability. LRS spectra of
52
53
54
55
56
57
58
59
60
61
62
63
64
65

these NPs (SI Fig. S7k) confirmed these findings, showing a significant increase in the intensity of the G, corresponding to the crystalline graphitic carbon, with respect to the D band, which is attributable to amorphous carbon, in the samples synthesized under *n*-BuOH, *t*-BuOH and CH₂OL. Moreover, these spectra did not show additional bands corresponding to iron carbide phases, excluding the development of surface carburization process during the ablation process at the tested conditions.

3.4. In situ coating of nZVI nanoparticles with hydrophilic molecules

Environmental and biomedical applications of nZVI particles require long-term water-dispersibility and no aggregation at pH in surface water systems (6.5 to 8.5), groundwater systems (6 to 8.5) and/or physiological buffers systems (~ 7.4). As mentioned above, EtOH-NPs transferred to DW showed good colloid stability at these pH values. Unfortunately, these dispersions, even those obtained from EtOH-NPs synthesized by using high vs values, showed hydrodynamic sizes and overall polydispersity index slightly larger than those considered suitable for environmental and biological applications. Therefore, to improve the water dispersibility and aggregation of these NPs, in situ coating with stabilizing hydrophilic molecules was performed by LA-PLA.

Experiments were carried out under the conditions used for Sample 1 but replacing DW with PEG (Sample 23) and aqueous solution (concentration 0.01 M) of water-soluble hydrophilic molecules [CA (Sample 21), PVP (Sample 22), and PEI (Sample 24)] as ablation media. TEM analysis revealed that such experiments yielded isolated and spherical NPs, showing a well-constructed core-shell structure (Fig. 6a to 6d), like NPs obtained under EtOH, but unlike DW-

NPs, where iron oxide nanoparticles embedded in an amorphous matrix of hematite were obtained.

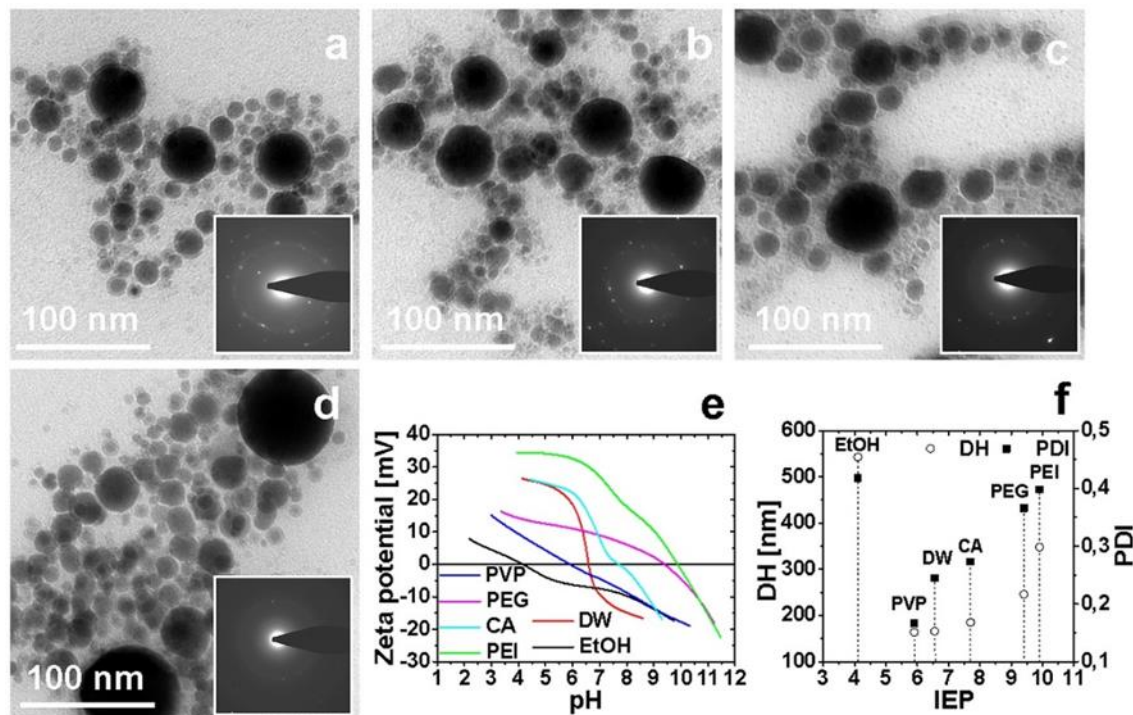


Fig. 6. TEM images and SAED of nZVI particles coated in situ with hydrophilic molecules: a) PVP; b) CA; c) PEG; d) PEI. Colloidal characterization of aqueous solutions of these NPs: e) zeta-potential curve as a function of pH; f) DH and PDIH values resulting from DLS analysis as a function of the isoelectric point (pH at which the zeta potential is zero). Data obtained for naked DW-NPs and EtOH-NPs transferred to DW are included in e) and f) for comparison.

Both the hydrodynamic size and the zeta potential were used to characterize the stability of the different suspensions of coated nZVI particles. These measurements were made at the original Fe concentrations estimated by TXRF for these samples, without dilution (46, 53, 60 and 69 $\text{mg} \cdot \text{L}^{-1}$ for PEG, CA, PVP and PEI coated-nZVI particles, respectively). In Fig. 6e, the zeta potential is plotted as a function of pH for NPs coated with PVP, CA, PEG and PEI respectively (that of naked NPs synthesized in DW and EtOH-NPs transferred to DW are included for comparison). As expected, the coating of nZVI particles with hydrophilic molecules shielded electrostatic charges on the particles, inducing a significant variation of the absolute values of the zeta

potential of the coated NPs at low and high pH, with respect to those measured for DW-NPs (6.5) and EtOH-NPs (4.1) transferred to DW. The zeta potential values variation implies that, in all cases, hydrophilic molecules were bound to the nZVI particle surface. At the same time, coated NPs had a shift in isoelectric point with respect to naked DW-NPs and EtOH-NPs transferred to DW. Thus, the presence of PEG and PEI molecules shifted strongly the isoelectric point of the nZVI particles to ~9.4 and ~9.9 respectively, showing good colloid stability at pH from 6 to 8.5. Regrettably, PEG and PEI coated NPs still showed higher *DH* (246 nm and 348 nm respectively) and *PDI_H* values (0.366 and 0.398 respectively) than those demanded for required for environmental and biomedical applications. On the other hand, the shift in the isoelectric point observed for NPs coated with PVP (~5.2) and CA (~7.6) was accompanied by a strong decrease in the *DH* (164 nm and 185 nm respectively) and *PDI_H* (0.167 and 0.273). Hence PVP and CA coated nZVI particles had good colloid stability and moderate hydrodynamic sizes and overall polydispersity index at physiological pH; therefore, they are ideal nanoprobe in biomedical applications. PVP-coated nZVI particles also had good water dispersibility and exhibited no aggregation at the pH found in surface and groundwater systems, this making them suitable for their use a reactive medium for degradation and removal of contaminants. Eventually, both *DH* and *PDI_H* values could probably be improved by means of laser pulse and target scanning parameters, as shown previously.

4. Conclusions

In this research, the pursue of optimal nanosecond LA-PLA conditions to obtain water stable colloidal dispersion of as-synthesized nanoscale ZVI particles from bulk iron targets were successfully tackled using both aqueous and non-aqueous ablation media. The use of ethanol as ablation media produced colloidal dispersions of iron–iron oxide core-shell nanoparticles coated

with amorphous carbon that exhibited a typical superparamagnetic behavior. The use of other alcohols produced similar nZVI particles with different degree of surface coating with carbonaceous products (amorphous carbon or crystalline graphite) and productivity, as a function of the hydrocarbon chain lengths and/or configuration of these alcohols. In addition, the size of these NPs decreased as the alcohol density and surface tension increased. Moreover, while the protective oxide shell was always formed by high crystalline Fe_3O_4 and/or $\gamma\text{-Fe}_2\text{O}_3$, the composition and crystalline order of the core changed with the wavelength of laser light and the NP size. When an infrared pulsed laser (1050 nm) was used, either an amorphous Fe phase (probably containing C atoms in its structure) or a BCC $\alpha\text{-Fe}$ phase was found, for NPs smaller or bigger than 30 nm, respectively. A well-crystallized iron carbide phase (Fe_3C) appeared when the iron targets were irradiated with visible pulsed laser (532 nm). In addition, a size boost (and a partial enhancement of the crystalline order in iron cores) could be achieved by increasing the energy and width of the laser pulses. Moreover, results showed that the size and width of the particle size distribution depended strongly on the pulse accumulation per spot, which is function of the pulse repetition rate and the scanning speed. Thus, the use of low pulse accumulation per spot values led to NPs populations with mean particle size and overall polydispersity index lower than 10 nm and 0.10, respectively, that were successfully transferred to deionized water, yielding stable water colloidal dispersions of nZVI with hydrodynamic size and polydispersity in the limit of those allowed for use in medicine or environmental remediation. Nanosecond LA-PLA in distilled water did not produce nZVI particles. Instead, it yielded ferromagnetic iron oxide nanoparticles (mainly Fe_3O_4 and $\gamma\text{-Fe}_2\text{O}_3$) included in a matrix of amorphous hematite, which showed low colloidal stability and high aggregation. Contrarily, experiments with polyethylene glycol and aqueous solutions of water-soluble hydrophilic molecules as ablation media, not only

1
2
3
4 produced core-shell nZVI particles like those obtained with alcohols, but also achieved in situ
5
6 coating of the as-synthesized nZVI particles with water soluble hydrophilic molecules,
7
8 improving their colloidal stability. In particular, in situ coating with citric acid and poly(-vinyl)
9
10 pyrrolidone yielded to colloidal dispersions of coated-nZVI particles showing good water
11
12 dispersibility and low aggregation suitable for their use in biomedical and/or environmental
13
14 applications. In summary, LA-PLA with target scanning has proven to be a successful method to
15
16 control the fabrication of stable nZVI colloids. The complete study has allowed identifying and
17
18 optimizing the critical parameters necessary to achieve a compromise between an interesting
19
20 ablation rate and the fulfillment of the particle size and stability objectives.
21
22
23
24
25

26 27 ASSOCIATED CONTENT

28
29
30 Supplementary data. File type PDF, which included two tables showing the Physical properties
31
32 of distilled water and the different alcohols used as solvents in the laser ablation in liquids
33
34 experiments; as well several artworks, which showed TEM, HRTEM and STEM images of the
35
36 NPS synthesized by changing the pulse laser wavelength (Figure S 2), the pulse energy (Figures
37
38 S 3 and S 4), the pulse width (Figure S 5), the pulse accumulation per spot (Figure s 6) and the
39
40 nature of the solvent (Figures S 1, S 7 and S 8).
41
42
43
44
45
46
47
48
49
50
51
52
53
54
55
56
57
58
59
60
61
62
63
64
65

TABLES

Table 1. Laser irradiation conditions used for the synthesis in pure distilled water (Sample 1) and ethanol (Samples 2-15), together with nanoparticle properties.

S ^{a)}	λ ^{b)} [nm]	P ^{c)} [W]	f ^{d)} [kHz]	τ_p ^{e)} [ns]	E _p ^{f)} [mJ]	F ^{g)} [J·cm ⁻²]	v _s ^{h)} [mm·s ⁻¹]	N ⁱ⁾	D _{TEM} ^{j)} [nm]	Sd _{TEM} ^{k)} [nm]	PDI ^{l)}	Ablation rate [mg _{Fe} L ⁻¹ h ⁻¹]	Fe content [mg _{Fe} ·mL ⁻¹]
1	1050	3.42	25	50	0.137	19.35	125	6.0	9.4	4.8	0.26	681	95
2	1050	3.42	25	50	0.137	19.35	125	6.0	13.5	9.5	0.50	408	57
3	532	3.42	25	50	0.137	19.35	125	6.0	12.4	9.2	0.54	466	65
4	1050	1.62	25	50	0.065	9.17	125	6.0	11.2	5.9	0.27	222	31
5	1050	5.35	25	50	0.214	30.28	125	6.0	21.5	16.8	0.61	452	63
6	1050	7.0	25	50	0.280	39.61	125	6.0	23.7	21.3	0.81	796	111
7	1050	5.35	25	8	0.214	30.28	125	6.0	13.1	8.4	0.41	208	29
8	1050	5.35	25	20	0.214	30.28	125	6.0	17.4	11.9	0.47	344	48
9	1050	5.35	25	100	0.214	30.38	125	6.0	24.1	21.3	0.78	488	68
10	1050	5.35	5	50	1.07	151.38	125	1.2	12.1	6.2	0.27	251	35
11	1050	5.35	15	50	0.356	50.46	125	3.6	15.8	10.8	0.46	402	56
12	1050	5.35	50	50	0.107	15.14	125	12	25.4	21.3	0.70	696	97
13	1050	5.35	25	50	0.214	30.28	500	1.5	12.4	7.4	0.35	251	35
14	1050	5.35	25	50	0.214	30.28	1000	0.8	8.9	4.4	0.25	172	24
15	1050	5.35	25	50	0.214	30.28	2500	0.3	7.8	2.5	0.10	143	20

^{a)} sample; ^{b)} laser wavelength; ^{c)} power of the laser beam; ^{d)} pulse repetition rate; ^{e)} pulse width; ^{f)} average pulse energy; ^{g)} pulse fluence; ^{h)} scanning speed; ⁱ⁾ pulse accumulation per spot; ^{j)} mean diameter obtained by TEM analysis; ^{k)} standard deviation; ^{l)} overall polydispersity index.

Table 2. Relevant physical properties at 25°C of the solvents used as ablation media, together with nanoparticle properties. [42]

S ^{a)}	Solvent	δ ^{b)} [g·mL ⁻¹]	σ ^{c)} [mN·m ⁻¹]	D _{TEM} ^{d)} [nm]	Sd _{TEM} ^{e)} [nm]	PDI ^{f)}	Dry weight [mg·L ⁻¹]	Fe content [mg _{Fe} ·mL ⁻¹]
1	Water (H ₂ O)	1.0	72.70	9.4	4.8	0.26	177	95
2	Ethanol (C ₂ H ₆ O)	0.7892	21.97	13.5	9.5	0.50	51	57
16	1-Propanol (C ₃ H ₈ O)	0.8037	23.30	12.6	8.7	0.47	80	46
17	2-Propanol (C ₃ H ₈ O)	0.7854	20.93	14.4	10.8	0.57	68	24
18	1-Butanol (C ₄ H ₁₀ O)	0.8097	24.57	11.7	7.4	0.40	269	27
19	tert-Butanol (C ₄ H ₁₀ O)	0.7886	20.70	18.4	14.9	0.66	277	6.3
20	Cyclohexanol (C ₆ H ₁₂ O)	0.962	34.40	10.9	6.3	0.33	286	4.6

^{a)} sample; ^{b)} density; ^{c)} surface tension; ^{d)} mean diameter obtained by TEM analysis; ^{e)} standard deviation; ^{f)} overall polydispersity index.

ACKNOWLEDGMENT

This research has been funded by the Spanish Ministry of Economy and Competitiveness (MINECO) and FEDER [research projects MAT2015-67354R, MAT2014-53961-R, and MAT2017-86826-R] and by the Aragón government (DGA) [grant for consolidated group PLATON E31_17R]. OBM thanks the financial support from the “Ramón y Cajal Program” [research project RYC-2010-07332] of the Spanish Ministry of Economy and Competitiveness (MINECO) and the H2020 Action H2020-MSCA-IF-2014_ST [grant 656908-NIMBLIS] of the Executive Agency for Research Manages of EU Commission. The Servicio General de Apoyo a la Investigación-SAI, Universidad de Zaragoza, is also acknowledged. R. Lahoz and O. Bomati contributed equally to this work.

ABBREVIATIONS

n-BuOH, 1-butanol; CH-OL, cyclohexanol; CA, citric acid; ICP-OES, Coupled Plasma-Optical Emission Spectrometry; DW, distilled water; EDS, Energy-Dispersive X-ray Spectroscopy; EELS, Electron Energy Loss Spectroscopy; EtOH, Cs-corrected STEM, Spherical Aberration Corrected Scanning Transmission Electron Microscopy; ethanol; FFT, Fast Fourier Transform; GIXRD, Grazing Incidence X-ray diffraction; HAADF, High Angle Annular Dark Field; DH, hydrodynamic size; High Resolution Transmission Electron Microscopy; HRTEM LRS, laser Raman spectroscopy; IEP, isoelectric point; LA-PLA, Liquid-Assisted Pulsed Laser Ablation; D_{TEM}, Mean Particle Diameter; NPs, Nanoparticles; nZVI, Nanoscale Zero-Valent Iron; ELNES, near-edge electron energy loss spectrum; PDI, Overall Polydispersity; PDI_H Index; overall DH polydispersity index PEG, Polyethylenglycol; PEI, Polyethylenimine; PVP, Poly(-vinyl) Pyrrolidone; 1-PrOH, 1-Propanol; 2-PROH, 2-Propanol; Sd_{DTEM}, Standard Deviation; SQUID, superconducting quantum interference device magnetometer; SPIONs, Superparamagnetic Iron Oxide Nanoparticles; STEM, Scanning Transmission Electron Microscopy; SAEDP, Selected Area Electron Diffraction Pattern; t-BuOH, tert-Butanol; TXRF, Total Reflection X-ray Fluorescence; TEM, Transmission Electron Microscope; and XPS, X-ray photoelectron spectroscopy.

REFERENCES

- [1] a) D.L. Huber. Synthesis, Properties, and Applications of Iron Nanoparticles. *Small*. 1, 5 (2005), 482-501, <https://doi.org/10.1002/sml.200500006>. b) O. Bomati-Miguel, M.P. Morales, P. Tartaj, J. Ruiz-Cabello, P. Bonville, M. Santos, S. Veintemillas-Verdaguer. Fe-based nanoparticulate metallic alloys as contrast agents for magnetic resonance imaging. *Biomaterials*, 26, 28 (2005) 5695-703, <https://doi.org/10.1016/j.biomaterials>. c) S. Cassim, S. A. Giustini, I. Baker, P. Hoopes. Development of Novel Magnetic Nanoparticles for Hyperthermia Cancer Therapy. *Proc SPIE* 7901 (2011) 70115 (1-8). <https://doi.org/10.1117/12.876514>.
- [2] C. Lee, J.Y. Kim, W.I. Lee, K.L. Nelson, J. Yoon, and D.L. Sedlak. Bactericidal Effect of Zero-Valent Iron Nanoparticles on Escherichia coli. *Environ Sci Technol*. 42, 13 (2008) 4927-4933. <https://doi.org/10.1021/es800408u>.
- [3] J.T. Nurmi, P.G. Tratnyek, V. Sarathy, D.R. Baer, J.E. Amonette, K. Pecher, M.D. Driessen. Characterization and Properties of Metallic Iron Nanoparticles: Spectroscopy, Electrochemistry and Kinetics. *Environ. Sci. Technol*. 39 (2005) 1221-1230. <https://doi.org/10.1021/es049190u>.
- [4] a) B. Karn, T. Kuiken, and M. Otto. Nanotechnology and in situ Remediation: A Review of the Benefits and Potential Risks. *Environ. Health Perspect*. 117, 12 (2009) 1813-1831. <https://doi.org/10.1289/ehp.0900793>. b) N.C. Mueller, J. Braun, J. Bruns, M. Cerník, P. Rissing, D. Rickerby, and B. Nowack. Application of Nanoscale Zero Valent Iron (NZVI) for Groundwater Remediation in Europe. *Environ. Sci. Pollut. Res*. 19 (2012) 550-558. <https://doi.org/10.1007/s11356-011-0576-3>. c) T.A. Bruton, B.F. Pycke and

- R.U. Haden. Effect of Nanoscale Zero-Valent Iron Treatment on Biological Reductive Dechlorination: A Review of Current Understanding and Research Needs. *Crit. Rev. Env. Sci. Tec.* 45, 11 (2015), 1148-1175. <https://doi.org/10.1080/10643389.2014.924185>.
- [5] R. Ajay Vasudeo, K. Krishnan, A. V.K, T. Sabu. Methods for Synthesis of Nanoparticles and Fabrication of Nanocomposites. *Micro and Nano Technologies: Synthesis of Inorganic Nanomaterials*. Woodhead Publishing, Elsevier, UKA (2018) 121-139.
- [6] M. Stefaniuk, P. Oleszczuk, and Y. Sik. Review on nano zerovalent iron (nZVI): From synthesis to environmental. *Chem. Eng. J.* 287 (2016) 618-632. <https://doi.org/10.1016/j.cej.2015.11.046>.
- [7] C.J. Choi, O. Tolochko, and B.K. Kim. Preparation of iron nanoparticles by chemical vapor condensation. *Mater. Lett.* 56, 3 (2002) 289-294. [https://doi.org/10.1016/S0167-577X\(02\)00457-3](https://doi.org/10.1016/S0167-577X(02)00457-3).
- [8] O. Bomati-Miguel, M.P. Morales, C. Serna, and S. Veintemillas-Verdaguer. Magnetic Nanoparticles Prepared by Laser Pyrolysis. *IEEE Trans. Magn.* 38, 5 (2002) 2216-2018. <https://doi.org/10.1109/INTMAG.2002.1001479>.
- [9] Z. Wang, X. Li, M. Gao, and X. Zeng. One-step preparation of amorphous iron nanoparticles by laser ablation. *Powder Technol.* 215–216 (2012) 147-150. <https://doi.org/10.1016/j.powtec.2011.09.039>.
- 10] S. Li, W. Yan, and W.X. Zhang. Solvent-free production of nanoscale zero-valent iron (nZVI) with precision milling. *Green Chem.* 11 (2009) 1618–1626. <https://doi.org/10.1039/b913056j>.

- [11] a) H. Zeng, X.W. Du, S.C. Singh, S.A. Kulinich, S. Yang, J. He, and W. Cai. Nanomaterials via Laser Ablation/Irradiation in Liquid: A Review. *Adv. Funct. Mater.* 22 (2012) 1333-1353. <https://doi.org/10.1002/adfm.201102295>. b) V. Amendola, and M. Meneghetti. What controls the composition and the structure of nanomaterials? *Phys. Chem. Chem. Phys.* 15 (2013) 3027-3046. <https://doi.org/10.1039/C2CP42895D>.
- [12] a) V. Amendola, P. Rielo, and M. Meneghetti. Magnetic Nanoparticles of Iron Carbide, Iron Oxide, Iron-Iron Oxide, and Metal Iron Synthesized by Laser Ablation in Organic Solvents. *J. Phys. Chem. C* 115, 12 (2011) 5140-5146. <https://doi.org/10.1021/jp109371m>. b) B. Kumar, and R.J. Tharejaa. Synthesis of nanoparticles in laser ablation of aluminum in liquid. *J. Appl. Phys.* 108 (2010) 064906 (1-6). <https://doi.org/10.1002/pssc.200983356>. c) T. Nakamura, H. Magara, Y. Herbani, and S. Sato. Fabrication of silver nanoparticles by highly intense laser irradiation of aqueous solution. *Appl. Phys. A* 104 (2011) 1021-1024. <https://doi.org/10.1007/s00339-011-6499-5>. d) Y. Jiang, P. Liu, Y. Liang, and G. Yang. Promoting the yield of nanoparticles from laser ablation in liquid. *Appl Phys A* 105 82011) 903-907. <https://doi.org/10.1007/s00339-011-6557-z>. e) M.R. Kim, J.Y. Kim, S.J. Kim, and D.J. Jang. Laser-induced fabrication of platinum nanoshells having enhanced catalytic and Raman properties. *Appl. Catal. A: General* 393 (2011) 317-322. <https://doi.org/10.1016/j.apcata.2010.12.013>. f) A.V. Simakin, V.V. Voronov, G.A. Shafeev, R. Brayner, and F. Bonzon-Verduraz. Nanodisks of Au and Ag produced by laser ablation in liquid environment. *Chem. Phys. Lett.* 348 (2001) 182-186. [https://doi.org/10.1016/S0009-2614\(01\)01136-8](https://doi.org/10.1016/S0009-2614(01)01136-8). g) G. Marzun, J. Nakamura, X. Zhang, S. Barcikowski, and P. Wagener. Size-control and supporting of palladium nanoparticles

- made by laser ablation in saline solution as a facile route to heterogeneous catalysts. Appl. Surf. Sci. 348, 1 (2015) 75-84. <https://doi.org/10.1016/j.apsusc.2015.01.108>. h) N.G. Semaltianos, S. Logothetidis, W. Perrie, S. Romani, R.J. Potter, S.P. Edwardson, K.G. Watkins. Silicon nanoparticles generated by femtosecond laser ablation in a liquid environment. J. Nanopart. Res. 12 (2010) 573-580. <https://doi.org/10.1007/s11051-009-9625-y>. i) J. Zang, and C.Q. Lan. Nickel and cobalt nanoparticles produced by laser ablation of solids in organic solution. Mater. Lett. 62 (2008) 1521-1524. <https://doi.org/10.1016/j.matlet.2007.09.038>. k) P. Wagener, A. Schwenke, B.N. Chichkov, and S. Barcikowski. Pulsed Laser Ablation of Zinc in Tetrahydrofuran: Bypassing the Cavitation Bubble. J. Phys. Chem. C. 114 (2010) 7618-7625. <https://doi.org/10.1021/jp911243a>. l) N. Lasemi, U. Pacher, L.V. Zhigilei, O. Bomati-Miguel, R. Lahoz R, W. Kautek. Appl. Surf. Sci. 433 (2018) 772-779. <https://doi.org/10.1016/j.apsusc.2017.10.082>. ll) N. Lasemi, O. Bomati Miguel, R. Lahoz, V.V. Lennikov, U. Pacher, C. Rentenberger, W. Kautek. Laser-Assisted Synthesis of Colloidal FeW_x O_y and Fe/Fex O_y Nanoparticles in Water and Ethanol. ChemPhysChem. 19 (2018) 1414-1419. <https://doi.org/10.1002/cphc.201701214>.
- [13] C.L. Sajti, R. Sattari, B.N. Chichkov and S. Barcikowski. Gram Scale Synthesis of Pure Ceramic Nanoparticles by Laser Ablation in Liquid. J. Phys. Chem. C. 114 (2010) 2421-2427. <https://doi.org/10.1021/jp906960g>.
- [14] a) L.A. Sukhov, A.V. Simakin, G.A. Shafeev, G. Viau and C. Garcia. Formation of nanoparticles during laser ablation of an iron target in a liquid. Quant. Electron. 42, 5 (2012) 453-456. <https://doi.org/10.1070/QE2012v042n05ABEH014753>. b) T. Iwamoto and T.J. Ishigaki. Fabrication of iron oxide nanoparticles using laser ablation in liquids.

- Phys. Conf. Ser. 441 (2013) 012034 (1-5). <https://doi.org/10.1088/1742-6596/441/1/012034>. c) A.I. Omelchenko, E.N. Sobol, A.V. Simakin, A.A. Serkov, I.A. Sukhov, and G.A. Shafeev. Biofunctional magnetic "core-shell" nanoparticles generated by laser ablation of iron in liquid. Laser Phys. 25 (2015) 025607 (1-5). <https://doi.org/10.1088/1054-660X/25/2/025607>.
- [15] a) G. Yang. Laser ablation in liquids: Applications in the synthesis of nanocrystals. Prog. Mat. Sci. 52 (2007) 648-698. <https://doi.org/10.1016/j.pmatsci.2006.10.016>. b) A. Simakin, V. Voronov, and G. Shafeev. Nanoparticle Formation During Laser Ablation of Solids in Liquids. Phys. Wave. Phenom., 14, 4 (2007) 218-240. <https://doi.org/10.3103/S1541308X07040024>. c) F. Taccogna, M. Dell'Aglia, G. Valenza, and A. De Giacomo. On the growth mechanism of nanoparticles in plasma during pulsed laser ablation in liquids. Plasma Sources Sci. Technol. 26, 4 (2017) 045002. <https://orcid.org/0000-0001-9361-9010>. d) M. Dell'Aglia, R. Gaudiuso, O. De Pascale, and A. De Giacomo. Mechanisms and processes of pulsed laser ablation in liquids during nanoparticle production. Appl. Surf. Sci. 348, 1 (2015) 4-9. <https://doi.org/10.1016/j.apsusc.2015.01.082>. e) D. Zhang, B. Gökce, and S. Barcikowski. Laser Synthesis and Processing of Colloids: Fundamentals and Applications. Chem. Rev. 117, 5 (2017) 3990–4103. <https://doi.org/10.1021/acs.chemrev.6b00468>.
- [16] M.E. Shaheen, J.E. Gagnon, and B.J. Fryer. Femtosecond laser ablation of brass in air and liquid media. J. Appl. Phys. 113 (2013) 213106-1(6). <https://doi.org/10.1063/1.4808455>.

- [17] K. O'Grady, and A. Bradbury. Particle size analysis in ferro-fluids. *J. Magnetism Magn. Mater.* 39 (1983) 91-94. [https://doi.org/10.1016/0304-8853\(83\)90407-9](https://doi.org/10.1016/0304-8853(83)90407-9).
- [18] International Centre for Diffraction Data. Powder Diffraction File™ (PDF®) 2018-2019, file JCPDS 89-0691. <http://www.icdd.com>: 2018.
- [19] International Centre for Diffraction Data. Powder Diffraction File™ (PDF®) 2018-2019, file. JCPDS 39-1346. <http://www.icdd.com>: 2018.
- [20] International Centre for Diffraction Data. Powder Diffraction File™ (PDF®) 2018-2019, file. JCPDS 04-014-0360. <http://www.icdd.com>: 2018.
- [21] a) M. Hanesch. Raman spectroscopy of iron oxides and (oxy)hydroxides at low laser power and possible applications in environmental magnetic studies. *Geophys. J. Int.* 177 (2009) 941-948. <https://doi.org/10.1111/j.1365-246X.2009.04122.x>. b) A.M. Jubb, and H.C. Allen. Vibrational Spectroscopic Characterization of Hematite, Maghemite, and Magnetite Thin Films Produced by Vapor Deposition *Appl. Mater. Interfaces.* 2, 10 (2010) 2804-2812. <https://doi.org/10.1021/am1004943>.
- [22] a) S. Reich, and C. Thomsen. Raman spectroscopy of graphite. *Phil. Trans. R. Soc. Lond. A.* 362 (2004) 2271–2288. <https://doi.org/10.1098/rsta.2004.1454>. b) N. Tarasenska, A. Stupak, N. Tarasenko, D. Mariotti, and S. Chakrabarti. Structure and optical properties of carbon nanoparticles generated by laser treatment of graphite in liquid. *ChemPhysChem.* 18, 9 (2017) 1074-1083. <https://doi.org/10.1002/cphc.201601182>.

- [23] Y. Yu, K. Lin, Z. Xiaoguo, W. Hua, L. Shilin, and M. Xingxiao. New C-H Stretching Vibrational Spectral Features in the Raman Spectra of Gaseous and Liquid Ethanol. *J. Phys. Chem. C*. 111 (2007) 8971- 8978. <https://doi.org/10.1021/jp0675781>.
- [24] E. Park, J. Zhang, S. Thomson, O. Ostrovski, and R. Howe, R. Characterization of Phases Formed in the Iron Carbide Process by X-Ray Diffraction, Mossbauer, X-Ray Photoelectron Spectroscopy, and Raman Spectroscopy Analyses. *Metall. Mater. Trans. B*. 32, 5 (2001) 840-845. <https://doi.org/10.1007/s11663-001-0071-1>.
- [25] M. Marton, M. Vojs, E. Zdravecká, M. Himmerlich, T. Haensel, S. Krischok, and R. Redhammer. Raman Spectroscopy of Amorphous Carbon Prepared by Pulsed Arc Discharge in Various Gas Mixtures. *J. Spectroscopy*. 467079 (2013) 1-6. <http://dx.doi.org/10.1155/2013/467079>.
- [26] Bomati-Miguel, O., Tartaj, P., Morales, M. P., Bonville, P., Golla-Schindler, U., Zhao, X. Q., and Veintemillas-Verdaguer, S. Core-Shell Iron-Iron Oxide Nanoparticles Synthesized by Laser-Induced Pyrolysis. *Small*. 2, 12 (2006) 1476-1483. <http://dx.doi.org/10.1002/sml.200600209>.
- [27] C. Colliex, T. Manoubi, and C. Ortiz. Electron-energy-loss-spectroscopy near-edge fine structures in the iron-oxygen system. *Phys. Rev. B*. 44, 20 (1991) 11402-11411. <https://doi.org/10.1103/PhysRevB.44.11402>.
- [28] U. Golla-Schindler, R. Hinrichs, O. Bomati-Miguel, and A. Putnis. Determination of the oxidation state for iron oxide minerals by energy-filtering TEM. *Micron*. 37 (2006) 473-477. <https://doi.org/10.1016/j.micron.2005.11.002>.

- [29] N. McIntyre and D. Zetaruk. X-ray photoelectron spectroscopy studies of iron oxides. Anal. Chem. 49, 11 (1977) 1521-1529. <https://doi.org/10.1021/ac50019a016>.
- [30] S. Moussa, G. Atkinson, and M. El-Shall. Laser-assisted synthesis of magnetic Fe/Fe₂O₃ core: carbon-shell nanoparticles in organic solvents. J. Nanopart. Res. 15, 3 (2013) 1470 (1-10). <https://doi.org/10.1007/s11051-013-1470-3>.
- [31] G.A. Parks. The isoelectric points of solid oxides, solid hydroxides, and aqueous hydroxo complex systems. Chem. Rev. 65, 2 (1965) 177-198. <https://doi.org/10.1021/cr60234a002>.
- [32] Y.-P. Sun, X.-Q. Li, J. Cao, Z. Wei-Xian, and H. Wang. Characterization of zero-valent iron nanoparticles. Adv. Colloid Interface Sci. 120 (2006) 47-56. <https://doi.org/10.1016/j.cis.2006.03.001>.
- [33] M. Kosmulski. pH-dependent surface charging and points of zero charge. IV. Update. J Colloid Interface Sci. 337 (2009) 439-448. <https://doi.org/10.1016/j.jcis.2009.04.072>.
- [34] P. Lichty, P. Kreider, O. Kilbury, D. King, W.W. Alan, M. Wirz, and D. Dinair. Surface Modification of Graphite Particles Coated by Atomic Layer Deposition and Advances in Ceramic Composites. Int. J. Appl. Ceram. Tec. 10, 2 (2013) 257-265. <https://doi.org/10.1111/j.1744-7402.2012.02750.x>.
- [35] B.D. Cullity. Introduction to Magnetic Materials. AddisonWesley Series in Metallurgy and Materials. Reading, Mass: Addison-Wesley Pub. Co. USA 1972.

- [36] A. Millan, A. Urtizberea, N. Silva, F. Palacio, V. Amaral, E. Snoeck, and V. Serin. Surface effects in maghemite nanoparticles. *J. Magnetism Magn. Mater.* 312, 1 (2007) L5-L9. <https://doi.org/10.1016/j.jmmm.2006.09.011>.
- [37] W.G. Mark, B.S. Myron, and S.S. Kenneth. Magnetic properties of amorphous iron. *Phys. Rev. B.* 48, 1 (1993), 269-273. <https://doi.org/10.1103/PhysRevB.48.269>.
- [38] Z. Nemati, J. Alonso, H. Khurshid, M. Phana, H. and Srikanth. Core/shell iron/iron oxide nanoparticles: are they promising for magnetic hyperthermia? *RSC Adv.* 6 (2016) 38697-38702. <https://doi.org/10.1039/C6RA05064F>.
- [39] A. Kanitz, J.S. Hoppius, M.M. Sanz, M. Maicas, A. Ostendorf, and E.L. Gurevich. Synthesis of magnetic nanoparticles by ultrashort pulsed laser ablation of iron in different liquids. *Chem Phys Chem.* 18, 9 (2017) 115-1164. <https://doi.org/10.1002/cphc.201601252>.
- [40] K.M. Krishnan. Biomedical Nanomagnetism: Spin Through Possibilities in Imaging, Diagnostics, and Therapy. *IEEE Trans Magn.* 46, 7 (2010) 2523–2558. <https://doi.org/10.1109/TMAG.2010.2046907>.
- [41] International Centre for Diffraction Data. Powder Diffraction File™ (PDF®) 2018-2019, file. JCPDS 00-035-0772. <http://www.icdd.com>: 2018.
- [42] NIST Chemistry WebBook, Standard Reference Data: <https://www.nist.gov/srd>.

<COPYRIGHT OWNER>
(hereinafter the "Copyright Owner")
JOURNAL PUBLISHING AGREEMENT

PLEASE PROVIDE US WITH THE FOLLOWING INFORMATION, REVIEW OUR POLICIES AND THE JOURNAL PUBLISHING AGREEMENT, AND INDICATE YOUR ACCEPTANCE OF THE TERMS

Article entitled: Pursuit of Optimal Synthetic Conditions for Obtaining Colloidal Zero-Valent Iron Nanoparticles by Scanning Pulsed Laser Ablation in Liquids

Corresponding author: Dr. Oscar Bomati-Miguel

To be published in the journal: Journal of Industrial and Engineering Chemistry

YOUR STATUS (PLEASE MARK ALL THAT APPLY)

☐ **I am the sole author of the manuscript**

Please indicate which of the below applies to you:

- ☐ I am a UK, Canadian or Australian Government employee and Crown Copyright is asserted
☐ I am a US Government employee and the Article is public domain and therefore the 'Assignment of copyright' clause does not apply
☐ I am a contractor of the US Government under contract number:
☐ None of the above

☒ **I am one author signing on behalf of all co-authors of the manuscript**

Please indicate which of the below applies to you:

- ☐ We are all US Government employees and the Article is public domain and therefore the 'Assignment of copyright' clause does not apply
☐ I am a US Government employee but some of my co-authors are not
☐ I am not a US Government employee but some of my co-authors are
☐ The work was performed by contractors of the US Government under contract number:
☐ All or some of the authors are UK, Canadian or Australian Government employees and Crown Copyright is asserted
☐ Some of the authors are employees of the UK, Canadian or Australian Government but Crown Copyright is not asserted
☒ None of the above

☐ **The Article is a 'work made for hire' and I am signing as an authorized representative and on behalf of my employer**

Please indicate which of the below applies to you:

- ☐ The Article is authored by US Government employees and the Article is public domain and therefore the 'Assignment of copyright' clause does not apply
☐ The work was performed by contractors of the US Government under contract number:
☐ The Article is authored by UK, Canadian or Australian Government employees and Crown Copyright is asserted
☐ None of the above

☐ **Signed on Behalf of Corresponding Author**

Please enter a valid email address.

Please complete this section if you are not the corresponding author as listed above. A copy of the agreement will be sent to you and the corresponding author.

- ☐ I am signing on behalf of the corresponding author
Name, job title and company (if employer representative)
E-mail address:.....

DATA PROTECTION & PRIVACY

I understand that staff of Elsevier and the publisher and its affiliated companies worldwide will be contacting me concerning the publishing of the Article and occasionally for marketing purposes (unless, with respect to such marketing, leave the box unticked).

- ☒ I do wish to receive news, promotions and special offers about products and services from Elsevier and the publisher and its affiliated companies worldwide

Please tick the above boxes (as appropriate), review the Journal Publishing Agreement, and then sign and date the document in black ink.

Signed: _____ Name printed: Oscar Bomati-Miguel

Title and Company (if employer representative): _____

Date: 26/07/2019

Please return the completed and signed original of this form by mail or fax, or by e-mailing a scanned copy of the signed original, retaining a copy for your files, to: oxfordcopyrights@elsevier.com

THE JOURNAL PUBLISHING AGREEMENT

Assignment of copyright

I hereby assign to the Copyright Owner the copyright in the manuscript identified above (where Crown Copyright is asserted, authors agree to grant an exclusive publishing and distribution license) and any tables, illustrations or other material submitted for publication as part of the manuscript (the “Article”). This assignment of rights means that I have granted to the Copyright Owner the exclusive right to publish and reproduce the Article, or any part of the Article, in print, electronic and all other media (whether now known or later developed), in any form, in all languages, throughout the world, for the full term of copyright, and the right to license others to do the same, effective when the Article is accepted for publication. This includes the right to enforce the rights granted hereunder against third parties.

Supplemental Materials

“Supplemental Materials” shall mean materials published as a supplemental part of the Article, including but not limited to graphical, illustrative, video and audio material.

With respect to any Supplemental Materials that I submit, the Copyright Owner shall have a perpetual worldwide non-exclusive right and license to publish, extract, reformat, adapt, build upon, index, redistribute, link to and otherwise use all or any part of the Supplemental Materials in all forms and media (whether now known or later developed), and to permit others to do so.

Research Data

“Research Data” shall mean the result of observations or experimentation that validate research findings and that are published separate to the Article, which can include but are not limited to raw data, processed data, software, algorithms, protocols, and methods.

With respect to any Research Data that I wish to make accessible on a site or through a service of the Copyright Owner, the Copyright Owner shall have a perpetual worldwide, non-exclusive right and license to publish, extract, reformat, index, adapt, build upon, redistribute, link to and otherwise use all or any part of the Research Data in all forms and media (whether now known or later developed), and to permit others to do so. Where I have selected a specific end user license under which the Research Data is to be made available on a site or through a service, the publisher shall apply that end user license to the Research Data on that site or service.

Reversion of rights

Articles may sometimes be accepted for publication but later rejected in the publication process, even in some cases after public posting in “Articles in Press” form, in which case all rights will revert to the author (see: <https://www.elsevier.com/about/our-business/policies/article-withdrawal>).

Revisions and addenda

I understand that no revisions, additional terms or addenda to this Journal Publishing Agreement can be accepted without the Copyright Owner’s express written consent. I understand that this Journal Publishing Agreement supersedes any previous agreements I have entered into with the Copyright Owner in relation to the Article from the date hereof.

Author Rights for Scholarly Purposes (see ‘Definitions’ clause below)

I understand that I retain or am hereby granted (without the need to obtain further permission) the Author Rights (see description below and definitions), and that no rights in patents, trademarks or other intellectual property rights are transferred to the Copyright Owner.

The Author Rights include the right to use the Preprint, Accepted Manuscript and the Published Journal Article for Personal Use and Internal Institutional Use. They also include the right to use these different versions of the Article for [Scholarly Sharing](#) purposes, which include sharing:

- the Preprint on any website or repository at any time;
- the Accepted Manuscript on certain websites and usually after an embargo period;
- the Published Journal Article only privately on certain websites, unless otherwise agreed by the Copyright Owner.

In the case of the Accepted Manuscript and the Published Journal Article the Author Rights exclude Commercial Use (unless expressly agreed in writing by the Copyright Owner), other than use by the author in a subsequent compilation of the author’s works or to extend the Article to book length form or re-use by the author of portions or excerpts in other works (with full acknowledgment of the original publication of the Article).

Author Representations/Ethics and Disclosure/Sanctions

I affirm the Author Representations noted below, and confirm that I have reviewed and complied with the relevant Instructions to Authors, Ethics in Publishing policy, Declarations of Interest disclosure and information for authors from countries affected by sanctions (Iran, Cuba, Sudan, Burma, Syria, or Crimea). Please note that some journals may require that all co-authors sign and submit Declarations of Interest disclosure forms. I am also aware of the publisher’s policies with respect to retractions and withdrawal (<https://www.elsevier.com/about/our-business/policies/article-withdrawal>). For further information see the publishing ethics page at <https://www.elsevier.com/about/our-business/policies/publishing-ethics> and the journal home page. For further information on sanctions, see <https://www.elsevier.com/about/our-business/policies/trade-sanctions>.

Author Representations

- The Article I have submitted to the journal for review is original, has been written by the stated authors and has not been previously published.
- The Article was not submitted for review to another journal while under review by this journal and will not be submitted to any other journal.
- The Article and the Supplemental Materials do not infringe any copyright, violate any other intellectual property, privacy or other rights of any person or entity, or contain any libellous or other unlawful matter.
- I have obtained written permission from copyright owners for any excerpts from copyrighted works that are included and have credited the sources in the Article or the Supplemental Materials.
- Except as expressly set out in this Journal Publishing Agreement, the Article is not subject to any prior rights or licenses and, if my or any of my co-authors’ institution has a policy that might restrict my ability to grant the rights required by this Journal Publishing Agreement

(taking into account the Author Rights permitted hereunder, including Internal Institutional Use), a written waiver of that policy has been obtained.

- If I and/or any of my co-authors reside in Iran, Cuba, Sudan, Burma, Syria, or Crimea, the Article has been prepared in a personal, academic or research capacity and not as an official representative or otherwise on behalf of the relevant government or institution.
- If I am using any personal details or images of patients, research subjects or other individuals, I have obtained all consents required by applicable law and complied with the publisher's policies relating to the use of such images or personal information. See <https://www.elsevier.com/about/our-business/policies/patient-consent> for further information.
- Any software contained in the Supplemental Materials is free from viruses, contaminants or worms.
- If the Article or any of the Supplemental Materials were prepared jointly with other authors, I have informed the co-author(s) of the terms of this Journal Publishing Agreement and that I am signing on their behalf as their agent, and I am authorized to do so.

Governing Law and Jurisdiction

This Agreement will be governed by and construed in accordance with the laws of the country or state of the Copyright Owner ("the Governing State"), without regard to conflict of law principles, and the parties irrevocably consent to the exclusive jurisdiction of the courts of the Governing State.

For information on the publisher's copyright and access policies, please see <http://www.elsevier.com/copyright>.

DEFINITIONS

Accepted Manuscript

The manuscript of an Article that has been accepted for publication and which typically includes author-incorporated changes suggested during submission, peer review, and editor-author communications. The Accepted Manuscript should not be added to or enhanced in any way to appear more like, or to substitute for, the Published Journal Article. The Accepted Manuscript should include a link to the formal publication through the relevant DOI and should bear a Creative Commons CC BY-NC-ND license.

Commercial Use

The use or posting of Articles:

- for commercial gain – for example by associating advertising with the full-text of the Article, by providing hosting services to other repositories or to other organizations, or charging fees for document delivery or access;
- to substitute for the services provided directly by the publisher – for example article aggregation, systematic distribution via e-mail lists or share buttons, posting, indexing or linking for promotional/marketing activities by commercial companies for use by customers and/or intended target audience of such companies (e.g. pharmaceutical companies and healthcare professionals/physician-prescribers).

Internal Institutional Use

Use by the author's institution for classroom teaching at the institution and for internal training purposes (including distribution of copies, paper or electronic, and use in coursepacks and courseware programs, but not in MOOCs – Massive Open Online Courses) and inclusion of the Article in applications for grant funding or for patent applications. For authors employed by companies, the use by that company for internal training purposes.

Personal Use

Use by an author in the author's classroom teaching (including distribution of copies, paper or electronic) or presentation by an author at a meeting or conference (including distribution of copies to the delegates attending such meeting), distribution of copies (including through e-mail) to known research colleagues for their personal use, use in a subsequent compilation of the author's works, inclusion in a thesis or dissertation, preparation of other derivative works such as extending the Article to book-length form, or otherwise using or re-using portions or excerpts in other works (with full acknowledgment of the original publication of the Article).

Preprint

Author's own write-up of research results and analysis that has not been peer reviewed, nor had any other value added to it by a publisher (such as formatting, copy editing, technical enhancements, and the like). Preprints should not be added to or enhanced in any way in order to appear more like, or to substitute for, the Published Journal Article.

Published Journal Article

The definitive final record of published research that appears or will appear in the journal and embodies all value-adding publisher activities including peer review co-ordination, copy-editing, formatting, (if relevant) pagination, and online enrichment.

Scholarly Sharing

Preprint: Sharing of Preprints by an author on any website or repository at any time. When the Article is accepted, the author is encouraged to include a link to the formal publication through the relevant DOI. The author can also update the Preprint on arXiv or RePEc with the Accepted Manuscript.

Accepted Manuscript:

- (i) **immediately on acceptance:** sharing of the Accepted Manuscript by an author:
 - via the author's non-commercial personal homepage or blog
 - via the author's research institute or institutional repository for Internal Institutional Use or as part of an invitation-only research collaboration work-group
 - directly by providing copies to the author's students or to research collaborators for their personal use
 - for private scholarly sharing as part of an invitation-only work group on commercial sites with which the publisher has a hosting agreement

- (ii) **after the embargo period:** an author may share the Accepted Manuscript via non-commercial hosting platforms (such as the author's institutional repository) and via commercial sites with which the publisher has a hosting agreement.

To check the embargo period for the journal, go to <http://www.elsevier.com/embargoperiodlist>.

The publisher has agreements with certain funding agencies that may permit shorter embargo periods and/or different sharing guidelines. To learn more about the publisher's policies and agreements with such agencies or institutions go to <http://www.elsevier.com/fundingbodyagreements>.

Published Journal Article: the author may share a link to the formal publication through the relevant DOI or may share the Published Journal Article privately with students or colleagues for their personal use, or privately as part of an invitation-only work group on commercial sites with which the publisher has a hosting agreement. Additionally theses and dissertations which contain embedded Published Journal Articles as part of the formal submission may be hosted publicly by the awarding institution with a link to the formal publication through the relevant DOI. Any other sharing of Published Journal Articles is by agreement with the publisher only.

For more information on the publisher's sharing policies please see <https://www.elsevier.com/sharingpolicy>.

Dear Editor,

Please, find enclosed the manuscript entitled: ‘Pursuit of Optimal Synthetic Conditions for Obtaining Colloidal Zero-Valent Iron Nanoparticles by Scanning Pulsed Laser Ablation in Liquids’, that we submit for its publication in “Journal of Industrial and Engineering Chemistry” and which is authored by Ruth Lahoz, Eva Natividad, Álvaro Mayoral, Christian Rentenberger, Daniel Díaz-Fernández, Eduardo J. Félix, Leonardo Soriano, Wolfgang Kautek and Oscar Bomati-Miguel, who has directed and coordinated this research. I acknowledge that I have consulted the Guide for Authors in preparing our submitted manuscript, and that I have prepared the manuscript in compliance with the Ethics in Publishing Policy.

State of the art:

Colloidal dispersions of Magnetic Nanoscale Zero-Valent Iron Particles (nZVI) particles have been intensely investigated in recent years due to their applications in biomedicine (such as magnetic resonance imaging contrast enhancement, and magnetic hyperthermia treatment), in the removal of contaminants presented in polluted ground-waters and soils and in catalysis. Therefore, development of efficient synthesis methods to meet the demand of these colloidal Fe metal nanoparticles is under intense research.

Nowadays, several bottom-up chemical methods are used to fabricate colloidal dispersions of nZVI particles for their application in biomedicine or environmental remediation and catalysis. However, the major issues of using chemical routes in solution are the serious drawbacks for large-scale manufacturing of metallic Fe nanoparticles, that make this processes long and expensive, and the generation of large amounts of intermediate products and impurities in both the nZVI particles and the colloidal suspensions. On the contrary, Liquid-Assisted Pulsed Laser Ablation (LA-PLA) is a

promising top-down method that allows a direct fabrication of colloidal dispersions of pure Fe metal nanoparticles in a cheap, simple and environmentally friendly manner.

The fabrication of nZVI particles by LA-PLA is not new. However, the literature has not agreed yet about the formation mechanisms of nanoparticles by LA-PLA and hence, about how to control simultaneously the four main outputs of laser synthesis of nanoparticles: size, composition, polydispersity and productivity. These variables are directly related with both the solvents used and especially the laser parameters, especially in the case of transition metals, which have different oxidation states and can give rise to different compounds depending on the nature and environmental conditions of the synthesis medium. Unfortunately, there are very few works in the scientific literature focused on the analysis of the influence of these parameters on the properties of the synthesized metal nanoparticles and the existing examples are focused only on the study of the production of noble metal NPs, whose composition and structure are not affected by the composition and nature of the solvent.

Novelty and impact:

Therefore, our work aims to provide a consensus to the scientific community by a systematic study of all the parameters affecting LA-PLA production of nZVI particles from iron massive precursors immersed in different liquids. One novelty is the complete and unusually thorough study of the chemical species present in these metallic Fe-based NPs with a wide battery of complementary techniques. Another distinguishing feature is that laser ablation was not performed on a fix target area as it is commonly done, but it was made with the laser beam scanning the target. This presents some advantages related to reproducibility and productivity. First, scanning allows minimizing the accumulation of laser pulses over damaged target areas. This accumulation varies both the chemical composition and the energy thresholds for ablation of the target. Second, scanning helps

keeping reasonably similar the local NP concentration of the liquid at the ablation site, given that the site changes, and also that scanning favours the dissipation of the synthesized NP cloud. Accordingly, both laser and scanning parameters were scoped and found to have different and relevant effects. A third distinctive mark is the deeper morphological and colloidal analysis of in-situ coated (with hydrophilic molecules) nZVI nanoparticles compared to other studies (e.g. with PVP or PEG), where only information about stability was mentioned. All this provides a well-supported discussion about the role of the different experimental parameters on the structure, composition, morphology, size and colloidal properties of the as-synthesized nanoparticles, and ultimately, a guide of optimal processing conditions to obtain stable aqueous colloidal dispersions of pure nZVI particles.

The authors consider that these findings take a further step towards efficient and environmentally friendly preparation of magnetic nanomaterials for different applications (i.e. biomedicine or environmental remediation applications) and, therefore, display so high impact as to deserve publication in Journal of Industrial and Engineering Chemistry. In this sense, it is important to point out that in the time interval 2015-2019, about 344 articles have been published in Journal of Industrial and Engineering Chemistry, which were focused on preparation or applications of magnetic nanoparticles. Moreover, we believe that these results fulfill the journal scope within the section “Nanomaterials and Nanostructural Engineering” and that the applied character of the nZVI particles was proved through magnetic and colloidal characterization. Moreover, the use of the laser ablation process in liquid for the synthesis of the pure metal Fe nanoparticles represent a clear example of the use of advanced and eco-friendly manufacturing technology to improve the existing synthesis iron nanoparticle process, which are traditionally used on an industrial and laboratory scale

Sincerely, and on behalf of all the authors,

Oscar Bomati-Miguel

RESPONSE TO REVIEWER #2.

The manuscript "Pursuit of Optimal Synthetic Conditions for Obtaining Colloidal Zero-Valent Iron Nanoparticles by Scanning Pulsed Laser Ablation in Liquids" present the variation in conditions to "optimize the production of nanoscale zero-valent iron (nZVI) particles suitable for biomedical or environmental applications using nanosecond LA-PLA on iron targets with different ablation media, laser and target scanning parameters". The authors present a serie of experiments and good characterization of the obtained material in each case. From my point of view, the results are very good and consistent with previous results (check "Chemical Physics Letters 512 (2011) 96-98").

We thank this reviewer for his/her positive comments about our present work.

The document describes very well the results of the characterization but throughout it, the initial objective is lost.

We agree with this reviewer with this point. This is why we have tried to transfer most of the characterization details to the SI. However, to address this point, we have clarified the objective at the end of the conclusions.

Some points require be clarified: 1) the principal application of the nanoparticles are biomedical but in the text the authors report carbonaceous material in the inner of the nanoparticle structure. Which is the influence of this material for these applications.

This reviewer is right to ask this question. In this sense, we have to indicate that, there are numerous published papers, which showed that the presence of carbon in Fe core-shell nanoparticles (either within the iron core in the form of a solid solution with the Fe or forming a shell on the particle surface) did not produce any adverse effect on the biocompatibility of these particles. In fact, the authors reference in this work one article published by Dr. O Bomati-Miguel (Biomaterials 26 (2005) 5695–5703) where a study of the biocompatibility and performance of magnetic resonance contrast agents of Fe core shell nanoparticles, whose core was composed by a solid solution between Fe an C, was conducted. In this paper, in vivo analysis demonstrated that the carbon content inside these particles did not produce any adverse effects on the analyzed animals (in this case mice). Similarly, the same author has published another article (Journal of Magnetism and Magnetic Materials 311 (2007) 120–124), where he analyzed the in vivo performance as a contrast agent for MRI of SiO₂-Fe core-shell nanoparticles included in an amorphous carbon matrix, obtaining similar results to those mentioned in the previous paper. That is, the presence of the carbon matrix surrounding the SiO₂-Fe particles did not produce any toxic effects in the analyzed animals (mice).

2) The authors use alcohols with different carbon numbers: which is the influence in the carbon number in the solvent in the carbon formation in the nanostructure.

Firstly, solvents with a high number of carbon atoms (J. Phys. Chem. B. 2005, 109, 23125–23128; Phys. Chem. Chem. Phys. 2013, 15, 3027–3046; J. Phys. Chem. C. 2011, 115, 5140–5146; J. Appl. Phys. 2010, 108, 034304) show pyrolysis on hot metal surfaces (in our case, the target). Therefore, one can assume that, for the same laser working parameters, each additional carbon atom inside the alcohol molecule leads to an increase of the alcohol

pyrolysis on the laser-irradiated target area, as well as on the surface of the generated nanoparticles. Therefore, there may be an increase in the absorption of carbon inside the nanoparticles core, or the appearance of more carbonaceous products on the particle surface. This effect is in good agreement with the increase in the nanoparticle carbon content observed in this paper from Fe nanoparticles synthesized under ethanol to Fe nanoparticles synthesized under cyclohexanol. Secondly, as it can be seen in Table 2 of this manuscript, a higher carbon chain length caused a decrease of the particle size and the width of the particle size distribution. This may be due to the hindrance of coalescence, a reduction of particle diffusion and possibly Ostwald ripening processes. However, this point is still under study. It is important to note that results presented in this work agree with those obtained for Drs. O. Bomati-Miguel, R. Lahoz and Prof.Dr. W. Kautek, where NPs of Ni were synthesized by laser ablation of a bulk Ni target under different alcohols (ChemPhysChem 2017, 18, 1118 – 1124).

3) The viscosity of the solvent is well known has a relevant impact in the particle size. Which is the viscosity of the solvent in each case.

This reviewer is right to point this out. However, we do not appreciate a clear impact of the viscosity in the particle size within the experimental viscosity range. The parameters that show an influence with a clear trend in the particle size (density and surface tension) are included in Table 2. Other solvent parameters whose influence has not a clear trend (among them, viscosity) are included in the SI Table S2.

4) The use of surfactants increase the stability and dispersability of the nanoparticles, the authors should clarify this point in their case. A maximum concentration or aggregation time should be addressed.

We agree with this reviewer with the fact that stability depends on concentration and time. In this work, we have not made a particular study on these parameters. The conclusion of that the use of surfactants increase the stability and dispersability is based on the IEP determination. In addition, compared to bare DW-NPs, which showed neither stability nor dispersability, the use of surfactants has played a clear role, since these dispersions remained stable for months. Moreover, we have clarified in the text that the value of the nanoparticle concentration used in the DLS experiments is the same than the one obtained in the synthesis, since no dilutions were made.

5) Finally, a table with the optimization values could help in the conclusions.

Certainly, a final set of optimized processing parameters would have been an outstanding and useful result. However, given the interconnected influence of the studied parameters, a specific set of values cannot be considered as sole optimum. For example, parameters used for the fabrication of nanoparticles with hydrophilic coatings are optimum for the particular E_p value used. After the complete study, a compromise within the different parameters should be taken in order to provide an interesting ablation rate that fulfills the particle size objectives. Later scalability of the process will require a modification of the E_p values and, consequently, the rest of parameters.

RESPONSE TO REVIEWER #3.

The authors, Lahoz et al. investigated an optimal condition for the synthesis of zero-valent iron nanoparticles (nZVI) by a liquid-assisted pulsed laser ablation method and studied its magnetic properties. Although it contains some interesting results, the structure of this manuscript is not clear enough. After careful evaluation of this manuscript, I recommend major revisions to improve the impact of the manuscript.

We thank this reviewer for his/her comments devoted to improve our present work. We hope to address correctly his/her revisions.

The following comments are helpful and consideration should be given to: 1. the authors should mention the results briefly in abstract, rather they have written like introduction as general.

After having critically reread the abstract with this reviewer's point of view, we agree that a modification is required, and we have done it consequently.

2. English grammar should be taken care of through the whole manuscript. For example, Line 16, of Page No. 3, the sentence "There are numerous reasons for this interest." looks the continuation is missing. Then, the abbreviation of LA-PLA has been mentioned in abstract, need not to be repeat it. For example, line 39 of page No. 4, etc.

According to this reviewer's concern, we have revised the entire document and corrected all issues.

3. The unit "ml" should be written as "mL" throughout the manuscript (see Page No. 12 of line 17 and 22).

Again, we agree with the reviewer. The unit "ml" has been corrected all over the text.

4. Authors mentioned the optimization process for the synthesis of nZVI, but authors obtained only mixed phase of iron oxides (γ -Fe₂O₃, Fe₃O₄ and -Fe).

We would like to clarify this appreciation from this reviewer. In the manuscript, we report NPs fabricated with several parameters. Apart from those NPs directly fabricated in DW and the smallest particles fabricated in other media (only a very small fraction of the total), which show only an iron oxide structure, the rest of the particles show an iron oxide-iron core-shell structure. Given the known difficulties of discerning magnetite and maghemite with the used characterization techniques, we always report both phases in the shell. However, the core is only Fe, as derived from spectroscopic studies. We think that maybe confusion can arise here since we have reported different compositions in the same dispersion, due to the polydispersity of the solution.

Is it possible to obtain pure nZVI phase using the PLA method? If that is so, what is the PLA optimal condition for the synthesis of nZVI?

Numerous authors, who are referenced in this manuscript, have previously established, that nanoscale zero-valent iron particle (nZVI) are nanoparticles, which exhibit a core-shell structure where a Fe(II)/Fe(III) oxide-oxihydroxide shell coats a Fe₀ core (Environ. Sci. Technol., 39, 1221-

1230; *Small*, 1 (5), 482–501; *Environ. Sci. Pollut. Res.*, 19, 550–558; *Chem. Eng. J.*, 287, 618–632; *Adv. Colloid Interface Sci.*, 120, 47–56; *Small*, 2 (12), 1476–1483). These composition is similar to those obtained in this paper. Therefore, it is possible to obtain pure nZVI nanoparticles. Consequently, the whole optimization study presented in this paper was focused in obtaining pure nZVI nanoparticles. Thus, core shell iron nanoparticles could be obtained by using alcohols as solvent or by using aqueous solutions (concentration 0.01 M) of water-soluble hydrophilic molecules (citric acid, poly(-vinyl) pyrrolidone K10 and polyethylenimine). Moreover, in the case of nanoparticles synthesized under alcohols, nanoparticles synthesized with ethanol showed the lowest carbon coating. Finally, nanoparticles synthesized by using higher scanning speed showed higher colloidal stability and narrow particle size distribution. Certainly, a final set of optimized processing parameters would have been an outstanding and useful result. However, given the interconnected influence of the studied parameters, a specific set of values cannot be considered as sole optimum. Therefore, that, an example of optimal conditions for the synthesis of nZVI particles are those, which involved: 1) the use of ethanol or aqueous solutions of water-soluble hydrophilic molecules as solvent. 2) Scanning speed velocities higher than 1000 mms⁻¹, to ensure obtaining a narrow size distribution. 3) Average laser pulse energy higher than 0.137, to obtain a sufficient production of nanoparticles. In sum, after the complete study, a compromise within the different parameters should be taken in order to provide an interesting ablation rate that fulfills the particle size objectives. Later scalability of the process will probably require a modification of parameters.

5. Although there are several synthetic methods available for synthesis of pure phase nZVI, what is the advantage of choosing the PLA method, since the authors obtained only with mixed phases and less amount of products via PLAL.

As already clarified in point 4, pure phase nZVI can be obtained by LA-PLA. Certainly, there are other synthetic methods available for this. However, LA-PLA presents several advantages, already cited in the introduction, over those methods. The most relevant are:

- LA-PLA is a simple top-down method to synthesize directly colloidal dispersions of nanoparticles
- Chemical precursors are replaced by much cheaper bulk raw materials which results in low cost and simplicity
- It is environmentally friendly: no necessity of applying large quantities of expensive surfactants and/or several synthetic steps to control the size, aggregation and colloidal stability of the synthesized nanoparticles
- It enables to reduce waste generation and operational costs: no production of large amounts of intermediate products and impurities in the final nZVI particles, avoiding multiple purification processes
- Continuous production with scale-up productivity can be achieved with no further process modification.

Moreover, further references to these and more advantages are found in the bibliography of this manuscript: *Phys. Chem. Chem. Phys.*, 15, 3027–3046; *Funct. Mater.* 22 (2012) 1333–1353; *Prog. Mat. Sci.* 52 (2007) 648–698.; *Chem. Rev.* 117, 5 (2017) 3990–4103.

6. In materials section 2.1; authors have mentioned "bulk -Fe phase" disk as a target for the PLA process. But in Results and Discussion, they mentioned as "bulk γ -Fe phase". Please check and provide a correct one.

As indicated by this reviewer, this error has been corrected.

7. Section 2.5, Page No. 9, line 19. What is the meaning of size around 2000 NPs? Is it about particle size? What is the unit? Generally, up to 100 nm size is called as NPs.

In the above sentence, the number "2000" refers to the number of analyzed particles and not to the size. Given that this sentence was not very clear, we have rewritten it as follows: "Particle size distribution was determined using a JEOL JEM1010 Transmission Electron Microscope (TEM) operated at 100 kV and a Philips CM200 at 200kV. For obtaining each size distribution, around 2000 NPs were analyzed using the Image J software. The obtained particle size distribution was lognormally fitted ..."

8. Fig.S2 of EDS spectrum, why are the Cu peaks shown? Authors should mention about the Cu peaks and the atomic or weight percentage of the element.

In contrast to the usual EDS characterization performed with SEM, in this case EDS is carried out by TEM. Therefore, the presence of Cu comes from the Cu grid holding the NPs.

9. "Conclusion" should be written as "Conclusions".

We agree with this reviewer.

10. Authors should check how the properties are changing after adding stabilizing agents. For example, how about the magnetic properties after coating of hydrophilic molecules with nZVI nanoparticles.

This reviewer's comment is certainly appropriate. Unfortunately, we do not have the data he/she suggests to include. Given the high number of samples required for this study, we decided to adjust as much as possible the amount of sample fabricated to the number and nature of the planned characterization studies. In addition, we did not envisaged magnetic characterization of nZVI nanoparticles coated in-situ with hydrophilic molecules. The reasons of this are several. First, TEM studies of these NPs revealed a great similitude with EtOH-NPs. Second, any influence the coating can have in the properties is certainly limited to the NP iron-oxide shell, whose contribution to the total magnetization is expected to be small. Third, in case that an influence in M or in hysteresis behavior is present, it could be masked or modified by other effects such as slight differences in size or size distribution between these samples. Forth, given that in the literature the studies on the effect of NP functionalization on magnetic properties are sometimes controversial (positive¹, negative² or none³) we consider that this particular subject deserves a careful and more advanced study well beyond the objective of section 3.4. Accordingly, this is certainly a study we should carry out in the near future.

¹ Estelle Silva Diorato Teixeira de Mendonça *et al.*, Surfaces and Interfaces, 14 (2019) 34-43

² R.P. Dhavale *et al.*, Journal of Colloid and Interface Science, 529 (2018) 415-425

³ M. Cîrcu *et al.*, Applied Surface Science 453 (2018) 457-463

11. The preparation method using a pulsed laser should be included in the Highlights

As suggested by this reviewer, we have changed first highlight to include the preparation method as follows:

- “nZVI particles fabricated by Liquid-Assisted Pulsed Laser Ablation by target scanning”

Supporting Information

Pursuit of Optimal Synthetic Conditions for Obtaining Colloidal Zero-Valent Iron Nanoparticles by Scanning Pulsed Laser Ablation in Liquids

*Ruth Lahoz, Eva Natividad**, Álvaro Mayoral, Christian Rentenberger, Daniel Díaz-Fernández, Eduardo J. Félix, Leonardo Soriano, Wolfgang Kautek, Oscar Bomati-Miguel**

SI Table S1

Properties at standard conditions	Deionized water (H ₂ O)	Ethanol (C ₂ H ₆ O)
Density, ρ [g/cm ³]	1.0	0.7892
Viscosity, η [cP]	0.894	1.074
Surface Tension, γ [mN/m]	72.70	21.97
Bulk modulus, K [GPa]	2,20	1,06
Longitudinal sound velocity, v_l [m/s]	1493	1207
Melting Temperature, T_m [K]	273.0	158.8
Boiling Temperature, T_{boil} [K]	373.2	351.5
Critical Temperature, T_c [K]	647	514
Critical density, ρ_c [g/cm ³]	0.322	0.276
Enthalpy of formation, $\Delta_f H^\circ_{liquid}$ [kJ/mol]	-285.8	-276.0
Enthalpy of vaporization, $\Delta_{vap} H^\circ$ [kJ/mol]	43.9	42.3
Heat capacity, $C_{p_{liquid}}$ [J/(molK)]	75.3	112.4
Heat conductivity, O [W/(mK)]	0.60	0.17
Refractive index, n_D (1064 nm)	1.326	1.3537
Absorption coefficient, α (1064 nm) [cm ⁻¹]	0.60588	0.12329

Table S1. Physical properties of deionized water and ethanol at standard conditions. The values of ρ , γ , η , v_l and K are listed from Kruusing (2008).¹ The values of T_m , T_{boil} , T_c , ρ_c , $\Delta_f H^\circ_{liquid}$, $\Delta_{vap} H^\circ$, $C_{p_{liquid}}$, and O are listed from Mallard (2016),². The values of α and n_D are listed from Polyanskiy (2014-2016).³

¹ A. Kruusing. Liquids and their properties. En A. Kruusing, Handbook of Liquids-Assisted Laser Processing (2008) 315-378. Amsterdam, The Netherlands: Elsevier Science. doi:978-0-08-044498-7

² W.G. Mallard (n.d.). NIST Chemistry WebBook. National Institute of Standards and Technology, Standard Reference Data Base. From <http://webbook.nist.gov/chemistry/>

³ M.N. Polyanskiy (2014-2016). Refractive index database. From <https://refractiveindex.info>.

SI Table S2

Sample	Solvent Properties							
	Solvent	δ^1 25 °C [g/mL]	BP ² [°C]	μ^3 25°C [cP]	σ^4 25°C [mN/m]	$\Delta fH^\circ_{\text{liquid}}{}^5$ 25°C [kJ/mol]	$\Delta v_{\text{ap}}H^\circ{}^6$ 25°C [kJ/mol]	$C_{p\text{liquid}}{}^7$ 25°C [J/mol*K]
1	water (H ₂ O)	1.0	99.9	0.89	72.70	-285.8	43.9	75.3
2	ethanol (C ₂ H ₆ O)	0.7892	78.2	1.07	21.97	-276.2	42.3	112.4
16	1-propanol (C ₃ H ₈ O)	0.8037	97.2	2.25	23.30	-302.5	47.0	144.6
17	2-propanol (C ₃ H ₈ O)	0.7854	82.3	2.22	20.93	-317.0	45.0	161.2
18	1-butanol (C ₄ H ₁₀ O)	0.8097	117.5	2.96	24.57	-328.0	52.0	176.9
19	tert-butanol (C ₄ H ₁₀ O)	0.7886	82.3	5.37	20.70	-359.2	46.0	298.2
20	cyclohexanol (C ₆ H ₁₂ O)	0.9620	161.8	56.20	34.40	-352.0	62.0	214.1

Table S2: Physical properties of distilled water and the different alcohols used as solvents in the laser ablation in liquids experiments: 1) density, 2) boiling point, 3) viscosity, 4) surface tension, 5) enthalpy of formation, 6) enthalpy of evaporation, 7) calorific capacity, 8) mean diameter obtained by TEM analysis, 9) Standard deviation, and 10) overall polydispersity index (NIST Chemistry WebBook, Standard Reference Data: <https://www.nist.gov/srd>).

SI Figure S1

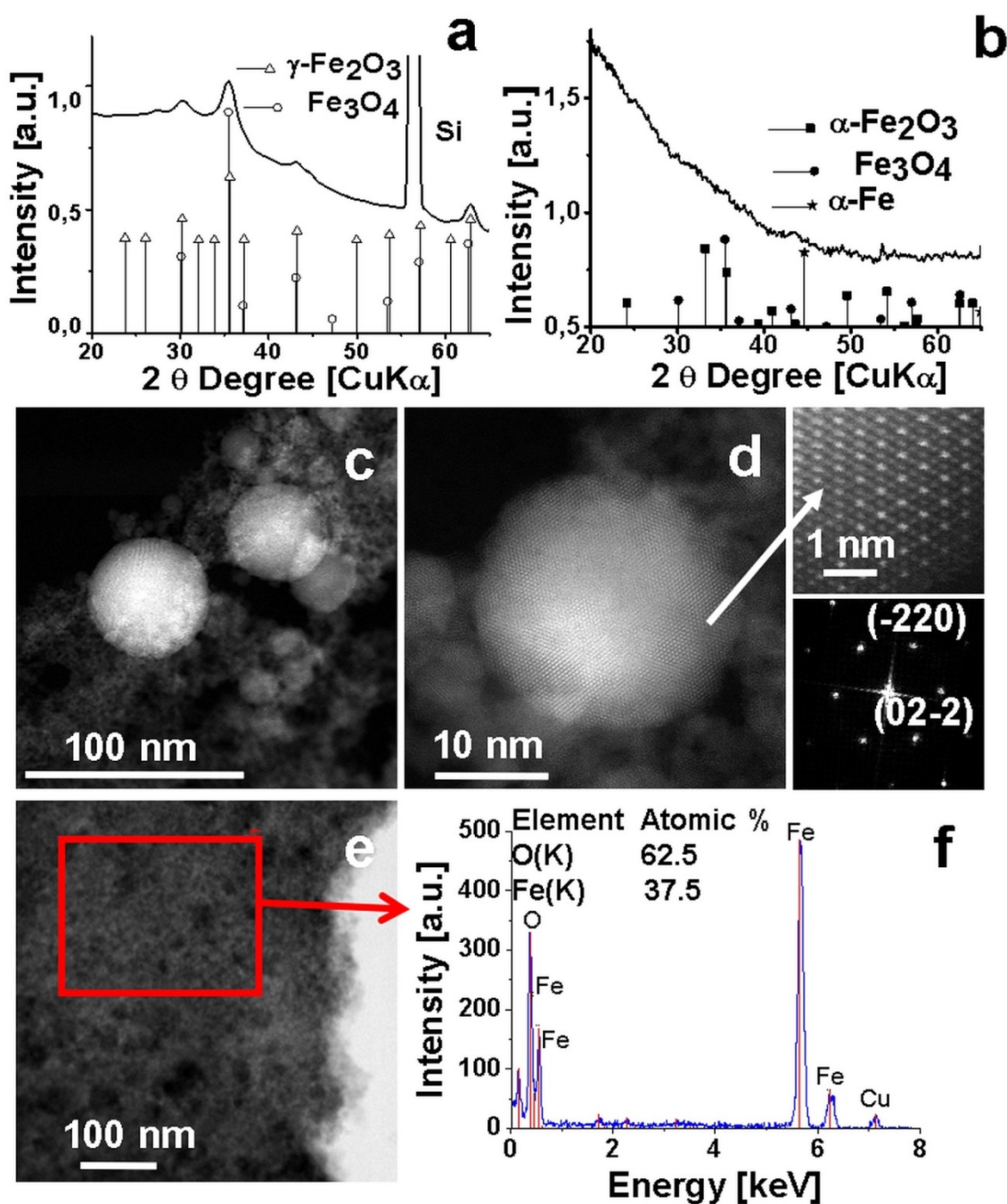


Figure S1: Structural and chemical characterization of nanoparticles synthesized by using deionized water (DW-NPs, Sample 1) or ethanol (EtOH-NPs, Sample 2) as solvent a) *GIXRD* spectra of a DW-NPs sample, revealing the existence of four broad peaks, corresponding to the (220), (311), (400) and (440) planes of a Fe₃O₄ or/and γ -Fe₂O₃ phase; b) *GIXRD* spectra of an EtOH-NPs sample, showing only very weak peaks related to a cubic γ -Fe₂O₃/Fe₃O₄ phase; c) STEM image of DW-NPs showing large nanoparticles embedded inside an amorphous matrix; d) high resolution STEM image of DW-NPs showing a large nanoparticle showing lattice fringes, together with detail of the lattice fringes (upper right) and obtained FFTs (bottom left), e) STEM image of the amorphous matrix presented in DW-NPs; and f) EDS spectra recorded in the area bounded by a red box in figure e.

SI Figure S1bis

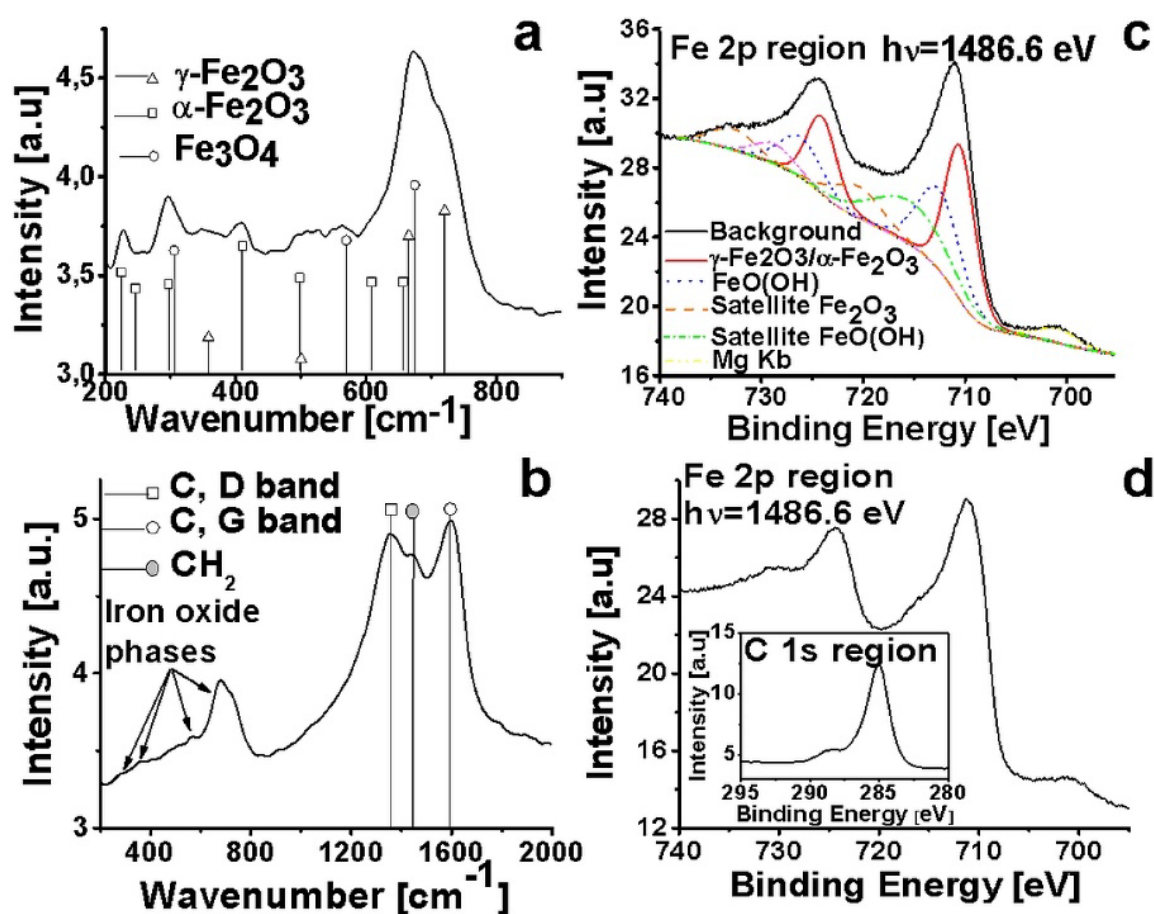


Figure S1bis: Detailed analysis of chemical characterization of DW-NPs (Sample 1) and EtOH-NPs (Sample 2).

a) LRS spectra of DW-NPs. A broad peak from 580 cm⁻¹ to 800 cm⁻¹ is observed, which consists of three components around 724 cm⁻¹, 673 cm⁻¹ and 660 cm⁻¹, corresponding to vibrational modes of *A*_{1g} symmetry of γ -Fe₂O₃/Fe₃O₄.^[4] This peak shows also a small shoulder at 600 cm⁻¹, which matches with a vibrational mode of *A*_{1g} symmetry of a FeO phase.^[4a] Additional peaks related to vibrational modes of *T*_{2g} symmetry were observed for Fe₃O₄ (310 cm⁻¹ and 560 cm⁻¹) or γ -Fe₂O₃ (310 cm⁻¹). Moreover, four peaks were detected at 228 cm⁻¹ (*A*_{1g}), 300 cm⁻¹ (*E*_g), 410 cm⁻¹ (*E*_g) and 500 cm⁻¹ (*A*_{1g}), which correspond to a α -Fe₂O₃ or a FeO(OH) phase.^[4b]

b) LRS spectra of EtOH-NPs. The spectrum shows several peaks around 365 cm⁻¹ (*T*_{2g}), 550 cm⁻¹ (*T*_{2g}) and 600 cm⁻¹ - 800 cm⁻¹ (*A*_{1g}), corresponding to γ -Fe₂O₃ or Fe₃O₄, and small shoulder at 590 cm⁻¹ - 600 cm⁻¹, related to FeO.^[4] Additionally, in EtOH-NPs two intense peaks are observed at 1360 cm⁻¹ (*A*_{1g}) and 1595 (*E*_{2g}) cm⁻¹, corresponding respectively to the D band of amorphous carbon materials and the G band of crystalline graphitic carbon.^[5] Moreover, a

⁴ a) M. Hanesch. Raman spectroscopy of iron oxides and (oxy)hydroxides at low laser power and possible applications in environmental magnetic studies. *Geophys. J. Int.* 177 (2009) 941-948. <https://doi.org/10.1111/j.1365-246X.2009.04122.x>. b) A.M. Jubb, and H.C. Allen. Vibrational Spectroscopic Characterization of Hematite, Maghemite, and Magnetite Thin Films Produced by Vapor Deposition Appl. Mater. Interfaces. 2, 10 (2010) 2804-2812. <https://doi.org/10.1021/am1004943>.

⁵ a) S. Reich, and C. Thomsen. Raman spectroscopy of graphite. *Phil. Trans. R. Soc. Lond. A.* 362 (2004) 2271-2288. <https://doi.org/10.1098/rsta.2004.1454>. b) N. Tarasenko, A. Stupak, N. Tarasenko, D. Mariotti, and S. Chakrabarti. Structure and optical properties of carbon nanoparticles generated by laser treatment of graphite in liquid. *ChemPhysChem.* 18, 9 (2017) 1074-1083. <https://doi.org/10.1002/cphc.201601182>.

smaller peak was observed at $\sim 1450\text{ cm}^{-1}$, which is related to $-\text{CH}_2$ groups from EtOH molecules physisorbed on the nanoparticles surface.^[6] Thus, the existence of iron carbide phases could be discarded due to the absence in this spectrum of an intense band at 2700 cm^{-1} (2D band), which is a characteristic feature of iron carbide.^[7]

c and d) XPS spectra of DW-NPs and EtOH-NPs, respectively. The analysis of the Fe2p region of both spectra showed the presence of two peaks about 710.7 eV and 724 eV, corresponding respectively to the Fe2p 3/2 and Fe2p 1/2 orbitals, and two broad peaks about 720 eV and 730 eV, corresponding respectively to the satellites of the Fe2p 3/2 and Fe2p 1/2 peaks. All these peaks are characteristic of the Fe^{3+} cations of the Fe_2O_3 .^[8] Additional peaks were observed close to 713.6 eV (Fe 2p 3/2), 726 eV (Fe2p 1/2) and a satellite peak at 716.6 eV, which are related to the Fe^{3+} cations of the iron (III) hydroxide ($\text{Fe}(\text{OH})_3$).^[8] The fact that no additional peaks related to the presence of Fe^{2+} or Fe were detected in EtOH-NPs was attributed to the analysis depth of XPS. Moreover, C1s spectrum of EtOH-NPs (inset in Figure 3d) showed the presence of three peaks close to 285 eV, 286.5 eV and 288.5 eV, which are related respectively to C-C bonding carbon bonds, C-O bonds from physisorbed EtOH molecules and $\text{C}\equiv\text{O}$ from physisorbed CO species.^[9,10] However, binding energies corresponding to iron carbide phases are not detected in this spectrum.

⁶ Y. Yu, K. Lin, Z. Xiaoguo, W. Hua, L. Shilin, and M. Xingxiao. New C-H Stretching Vibrational Spectral Features in the Raman Spectra of Gaseous and Liquid Ethanol. *J. Phys. Chem. C* 111 (2007) 8971- 8978. <https://doi.org/10.1021/jp0675781>.

⁷ G.A. Parks. The isoelectric points of solid oxides, solid hydroxides, and aqueous hydroxo complex systems. *Chem. Rev.* 65, 2 (1965) 177-198. <https://doi.org/10.1021/cr60234a002>.

⁸ N. McIntyre and D. Zetaruk. X-ray photoelectron spectroscopy studies of iron oxides. *Anal. Chem.* 49, 11 (1977) 1521-1529. <https://doi.org/10.1021/ac50019a016>.

⁹ M. Marton, M. Vojs, E. Zdravceková, M. Himmerlich, T. Haensel, S. Krischok, and R. Redhammer. Raman Spectroscopy of Amorphous Carbon Prepared by Pulsed Arc Discharge in Various Gas Mixtures. *J. Spectroscopy*. 467079 (2013) 1-6. <http://dx.doi.org/10.1155/2013/467079>.

¹⁰ S. Moussa, G. Atkinson, and M. El-Shall. Laser-assisted synthesis of magnetic Fe/Fe₂O₃ core: carbon-shell nanoparticles in organic solvents. *J. Nanopart. Res.* 15, 3 (2013) 1470 (1-10). <https://doi.org/10.1007/s11051-013-1470-3>.

SI Figure S2

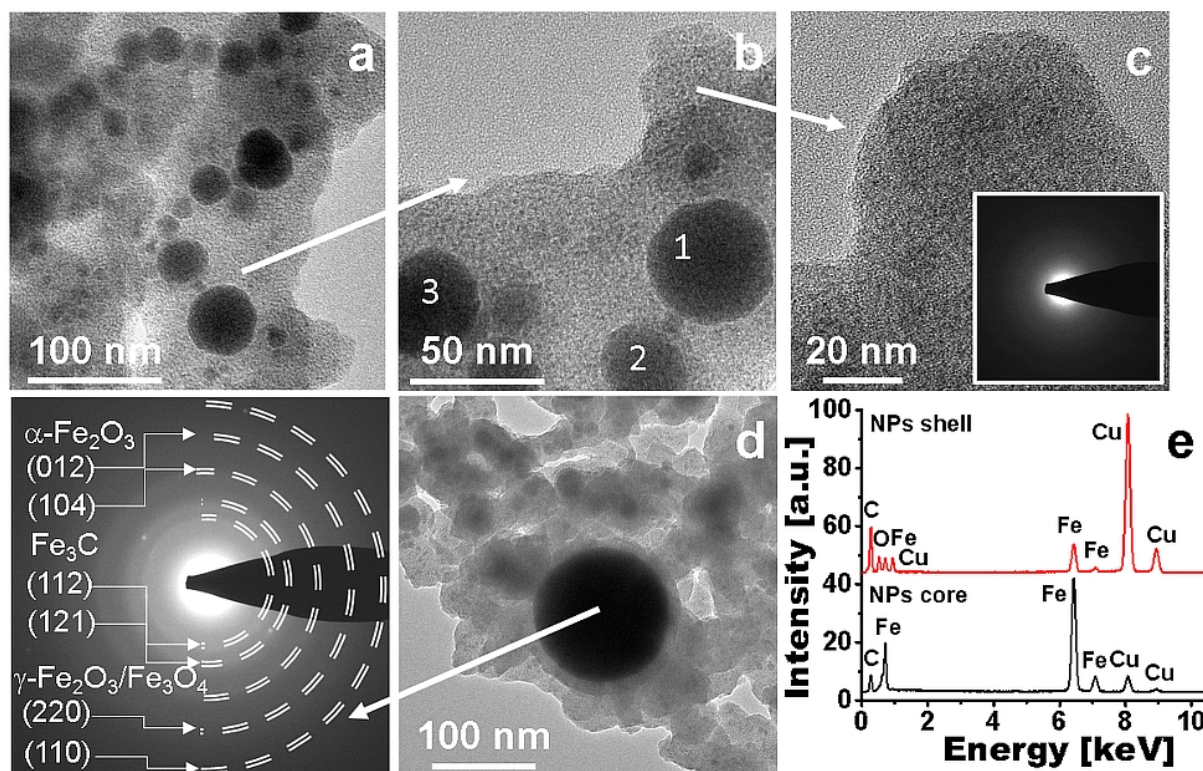


Figure S2: Characterization of EtOH-NPs synthesized by using a visible pulsed-laser (Sample 3). a) Low magnification TEM image; b) High magnification TEM images of an area displayed in image a, showing nanoparticles; c) HRTEM of an area of the matrix showed in image a (inset: SAED pattern of these area); d) HRTEM image of a large nanoparticle together with obtained SAED pattern); e) EDS spectra recorded for the shell and the core of the nanoparticle displayed in figure d).

SI Figure S3

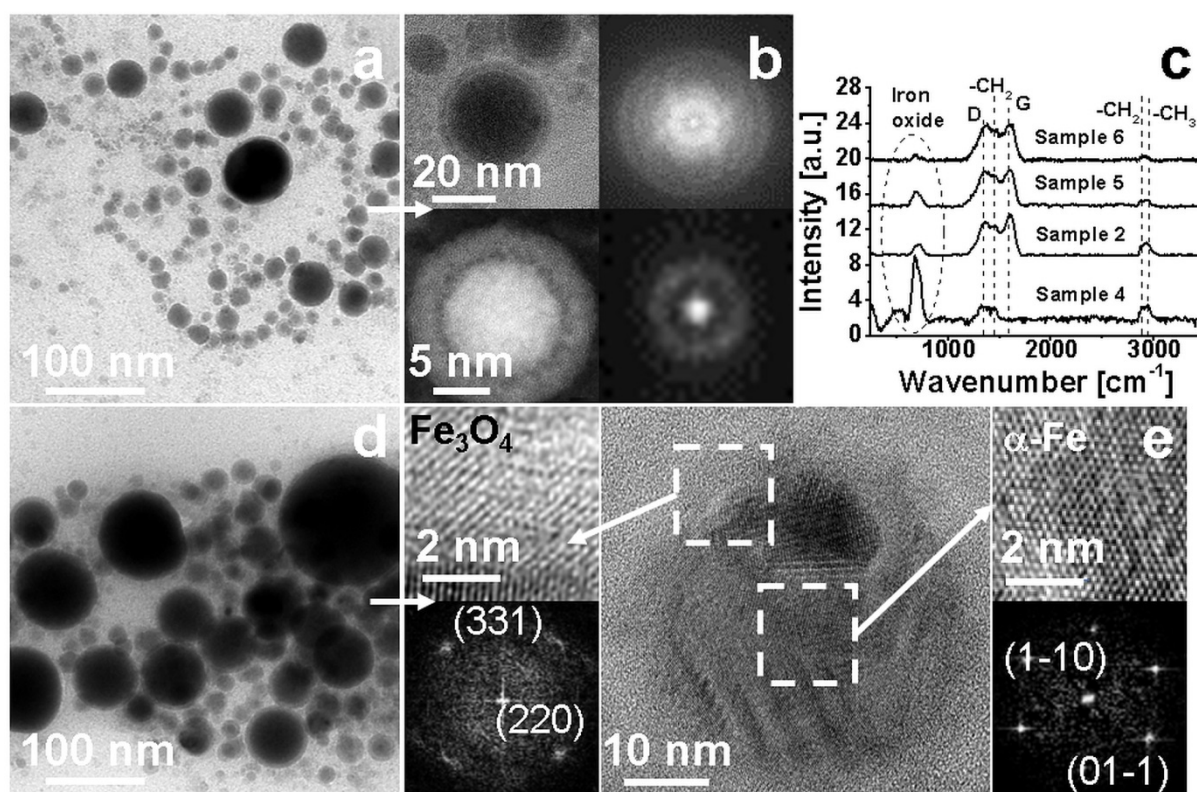


Figure S3: TEM and LRS analysis of nanoparticles synthesized by changing the pulse energy: a) Sample 4, synthesized at 0.065 mJ; b) HRTEM images together with obtained FFTs patterns of NPs displayed in image a; c) LRS spectra of the as-synthesized NPs, from top to bottom, Sample 6, Sample 5, Sample 2 and Sample 1; d) Sample 6, synthesized at 0.280 mJ; e) HRTEM images together with obtained FFTs patterns of the shell and core of a NPs showed in figure d.

SI Figure S4

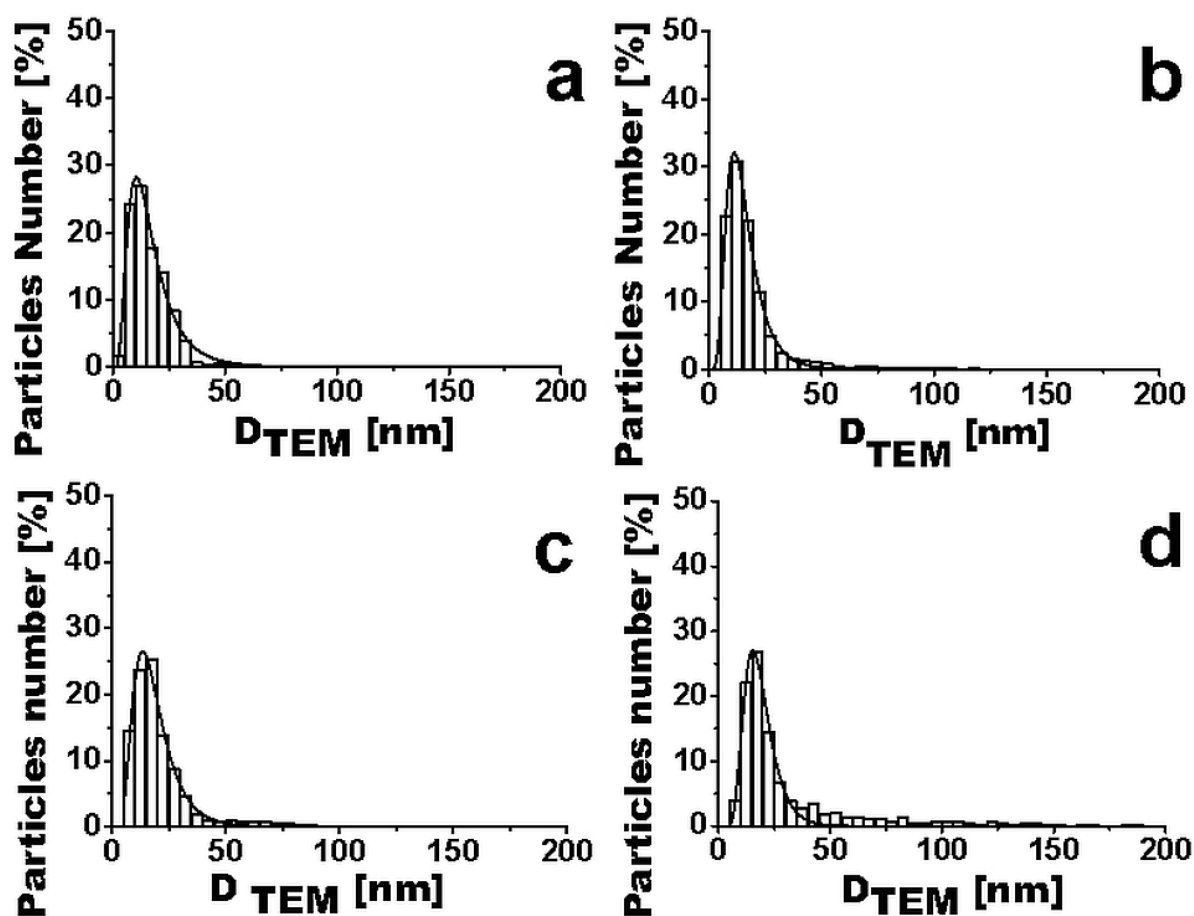


Figure S4: Particle size distribution of nZVI particles synthesized by changing the pulse energy and, consequently, the fluence: a) Sample 4, $9.17 \text{ J} \cdot \text{cm}^{-2}$; b) Sample 2, $19.4 \text{ J} \cdot \text{cm}^{-2}$; c) Sample 5, $30.3 \text{ J} \cdot \text{cm}^{-2}$; and d) Sample 6, $39.61 \text{ J} \cdot \text{cm}^{-2}$.

SI Figure S5

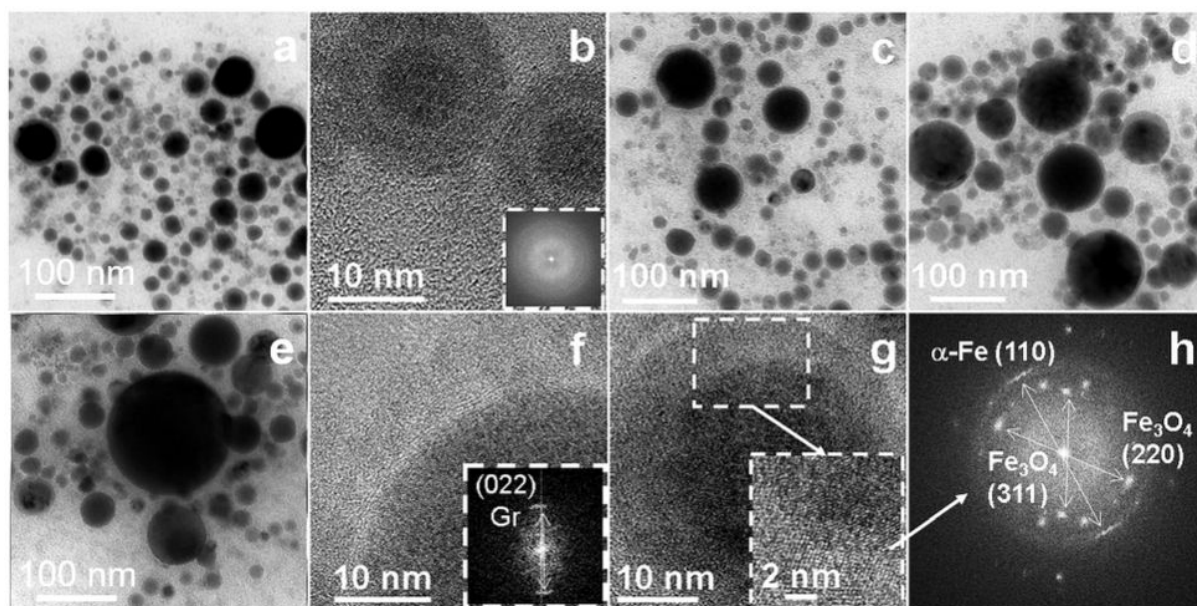


Figure S5: TEM analysis of nanoparticles synthesized in EtOH by changing the pulse width: a) Sample 7, $\tau_p = 8$ ns; b) HRTEM image and FFT pattern of core-shell nanoparticle synthesized at $\tau_p = 8$ ns, showing amorphous cores; c) Sample 8, $\tau_p = 20$ ns ; d) Sample 2, $\tau_p = 50$ ns; e) Sample 9, $\tau_p = 100$ ns; f) HRTEM image of a core-shell nanoparticle synthesized at $\tau_p = 100$ ns, showing an outer layer of crystalline graphite; g) HRTEM image of a core-shell nanoparticle synthesized at $\tau_p = 100$ ns showing discernible lattice fringes in the shell and the core; and h) FFT pattern of the magnified area, which is framed in white in figure g.

SI Figure S6

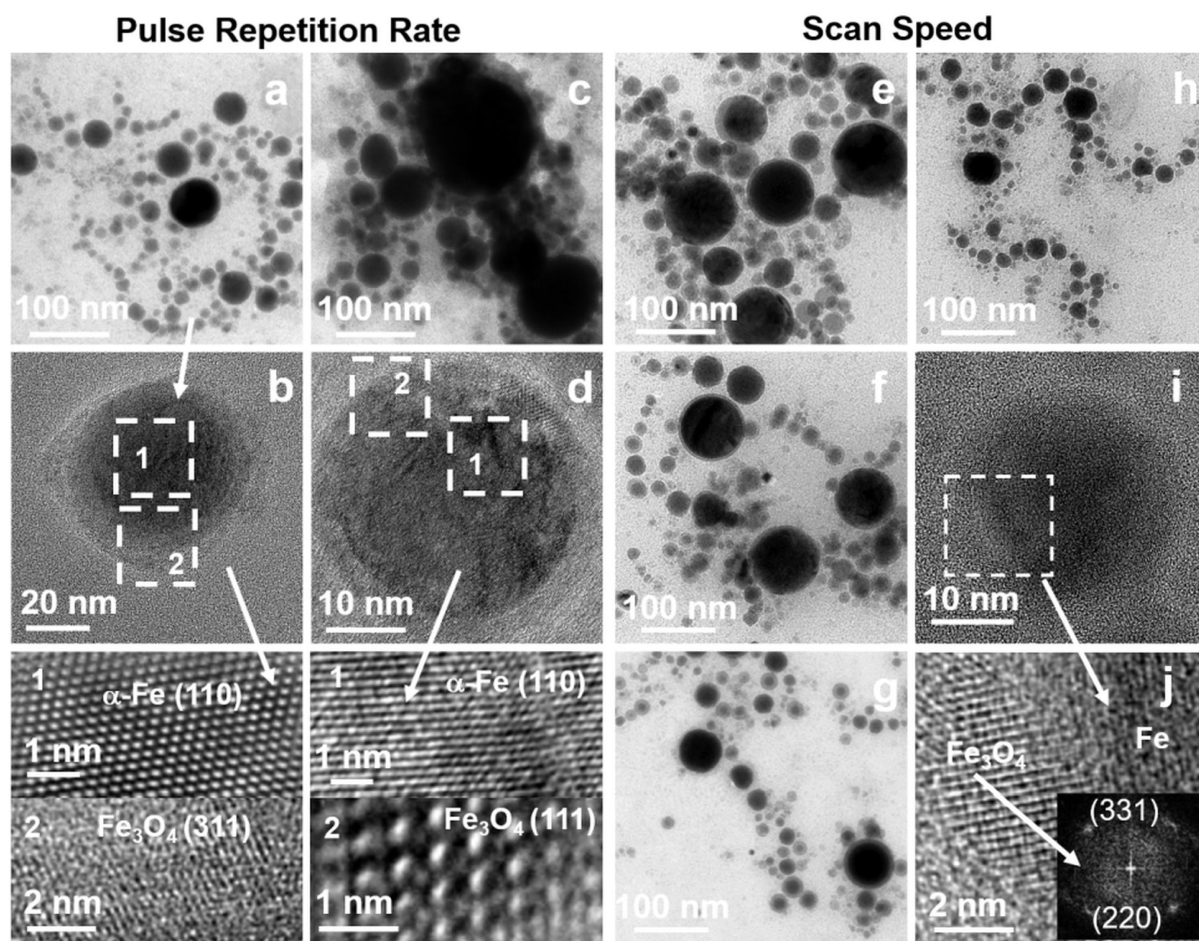


Figure S6: TEM analysis of EtOH-NPs synthesized by changing the pulse accumulation per spot with the pulse repetition rate (left) and the scan speed (right): a) Sample 10, $f = 5$ kHz; b) HRTEM image of a core-shell nanoparticle synthesized at $f = 5$ kHz, showing an outer layer of iron oxide (zoom 2) and a core of crystalline iron (zoom 1); c) sample 12, $f = 50$ kHz; d) HRTEM image of nanoparticle synthesized at $f = 50$ kHz, showing an iron core (zoom 1)-oxide shell (zoom 2) structure; e) sample 5, $v_s = 125 \text{ mm} \cdot \text{s}^{-1}$; f) sample 13, $v_s = 500 \text{ mm} \cdot \text{s}^{-1}$; g) Sample 14, $v_s = 1000 \text{ mm} \cdot \text{s}^{-1}$; h) sample 15, $v_s = 2500 \text{ mm} \cdot \text{s}^{-1}$; i and j) HRTEM images of a core-shell nanoparticle synthesized at $v_s = 2500 \text{ mm} \cdot \text{s}^{-1}$, showing an outer layer of iron oxide and a core of crystalline iron together with obtained FFTs patterns.

SI Figure S7

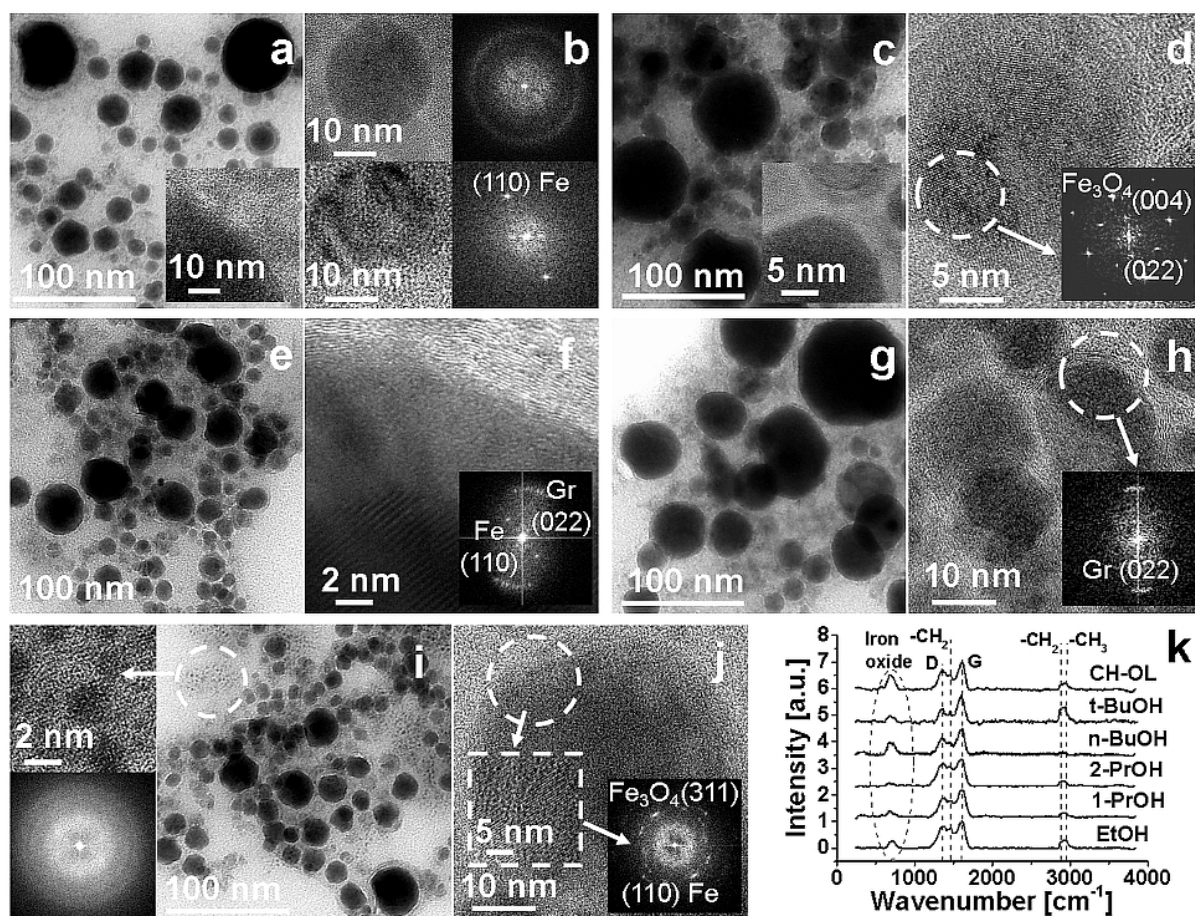


Figure S7: TEM and LRS characterization of iron-iron oxide core-shell nanoparticles synthesized by using different alcohols as solvent: a) core-shell NPs synthesized under *l*-PROH (Sample 16) partially coated with a carbonaceous matrix (zoom); b) HRTEM images of NPs synthesized under *l*-PROH showing amorphous (upper left) and crystalline (bottom left) iron cores, together with the obtained FFTs patterns (right images); c) NPs synthesized under 2-PROH (Sample 17) showing an external layer of amorphous carbon; d) HRTEM of a NPs synthesized under 2-PROH showing an outer layer of iron oxide, together with the obtained FFTs patterns (inset); e) NPs synthesized by using *n*-BuOH as solvent; f) detail of a large NPs synthesized under *n*-BuOH showing a crystalline core with lattice fringes and detail of a graphitic outer layer, together with the obtained FFT patterns (inset); g) NPs synthesized under *t*-BuOH; h) HRTEM image of NPs synthesized under *t*-BuOH showing graphitic outer layer, together with the obtained FFTs patterns (inset); i) TEM image of NPs synthesized under CH-OL showing small carbon NPs (left top zoom) together with the FFT patterns (left bottom zoom) obtained for these carbon NPs; j) HRTEM image of a large NPs synthesized under CH-OL showing an outer shell of crystalline iron oxide and a core of crystalline iron (zoom), together with the obtained FFT patterns (inset); k) LRS spectra of the synthesized nanoparticles (Raman spectrum of sample synthesized under EtOH is included for comparison).

SI Figure S8

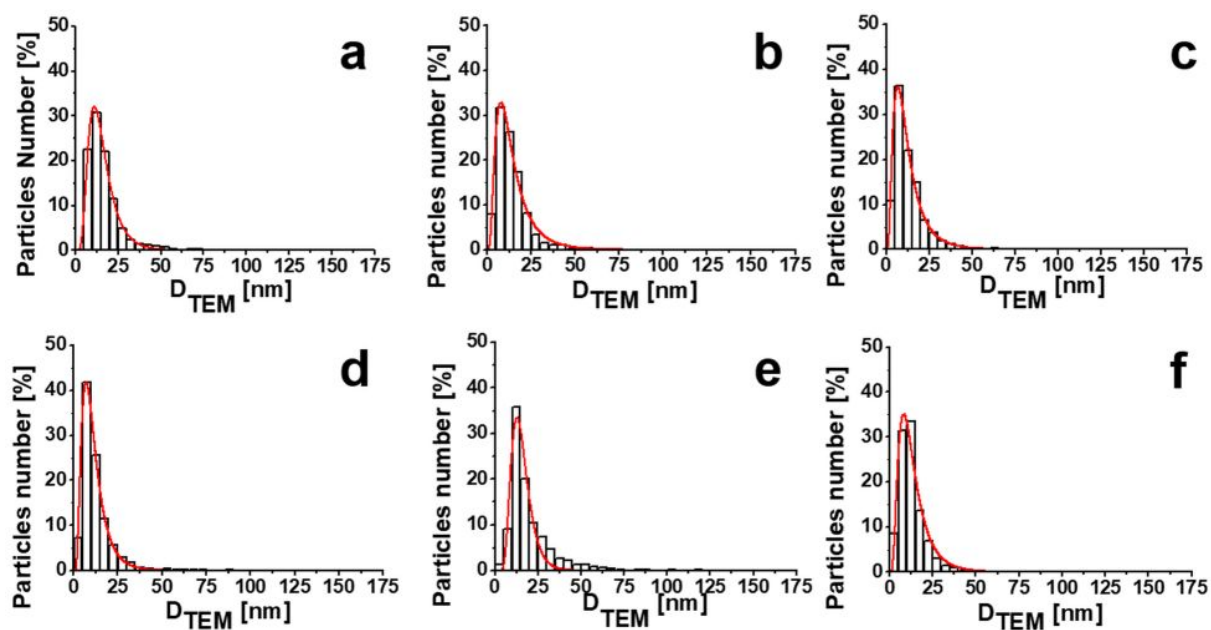
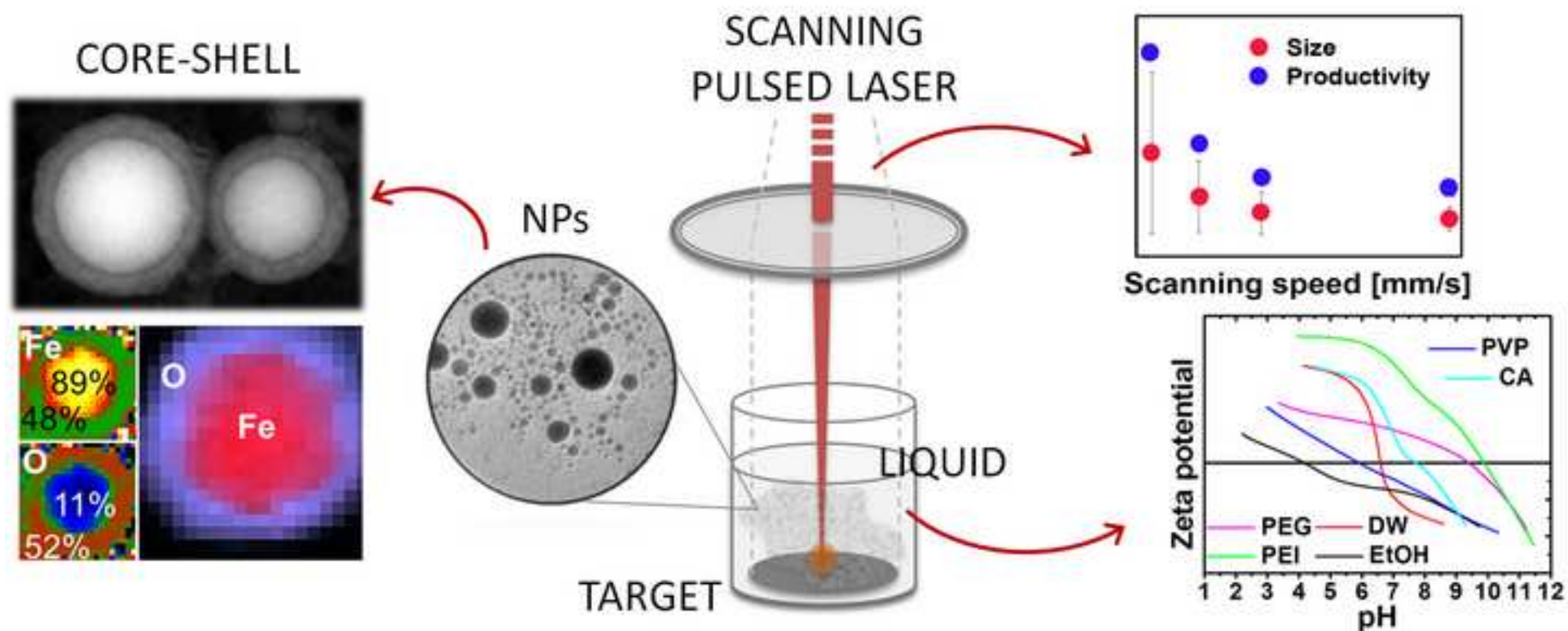


Figure S8: Particle size distribution of nZVI particles synthesized by using different alcohols: a) ethanol, b) *l*-propanol, c) 2-propanol, d) *l*-butanol, e) *tert*-Butanol, and f) cyclohexanol.



Highlights

- nZVI particles fabricated by Liquid-Assisted Pulsed Laser Ablation by target scanning
- In situ citric acid and PVP coating gives good dispersibility and low aggregation
- Alcohol density and surface tension govern NP size, while chain length productivity
- Core composition and crystalline order vary with laser wavelength and NP size
- Energy, width and especially pulse accumulation govern NP size and polydispersity

Figure

[Click here to download high resolution image](#)

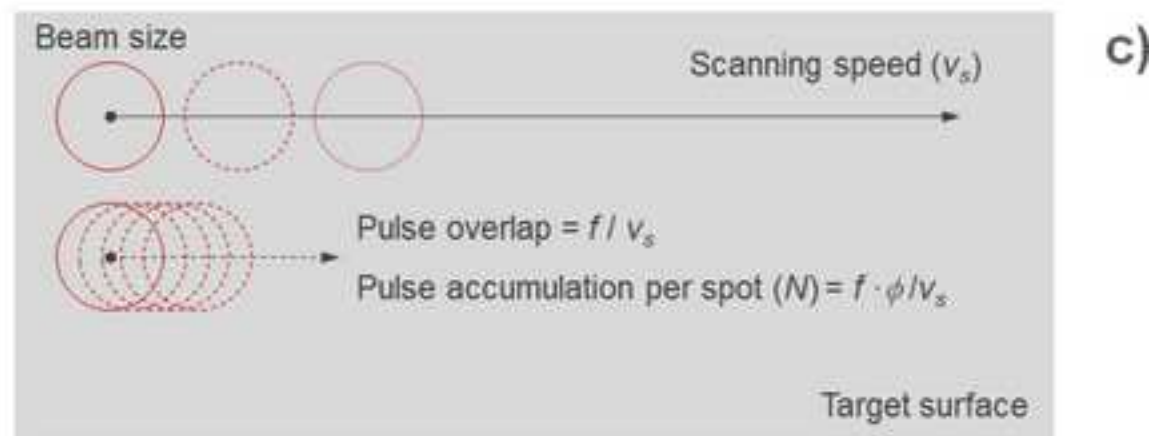
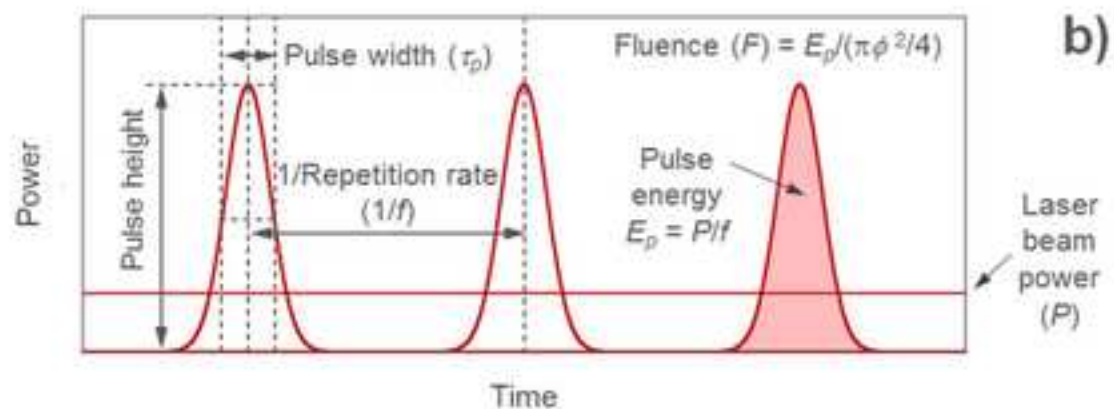
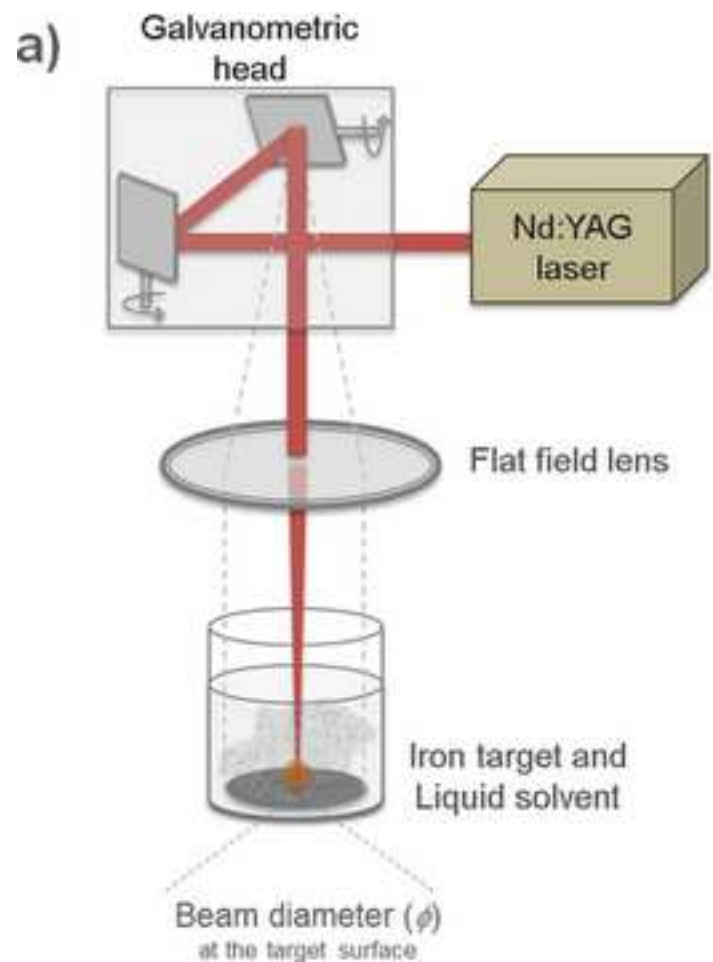
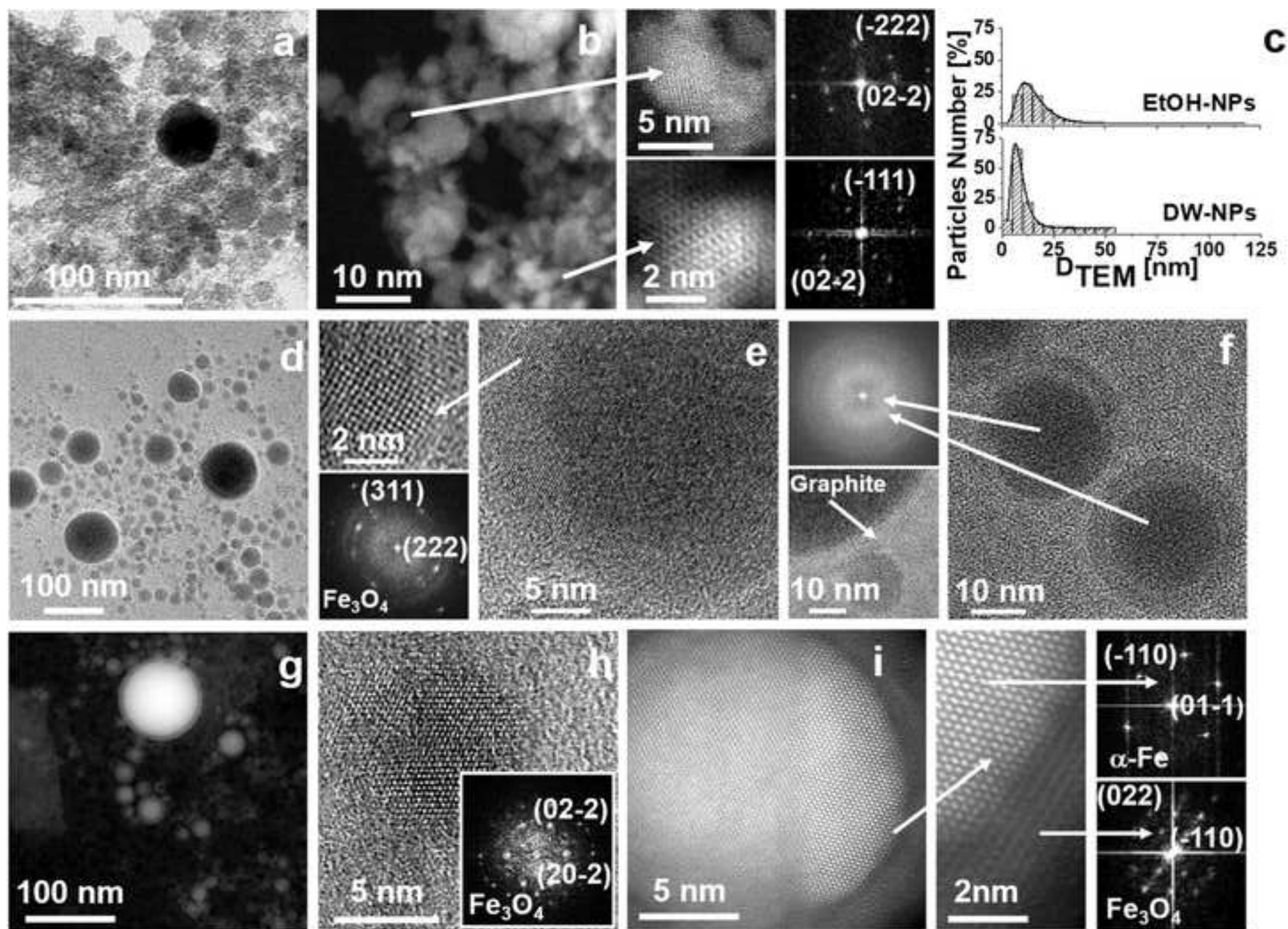


Figure
[Click here to download high resolution image](#)



Figure

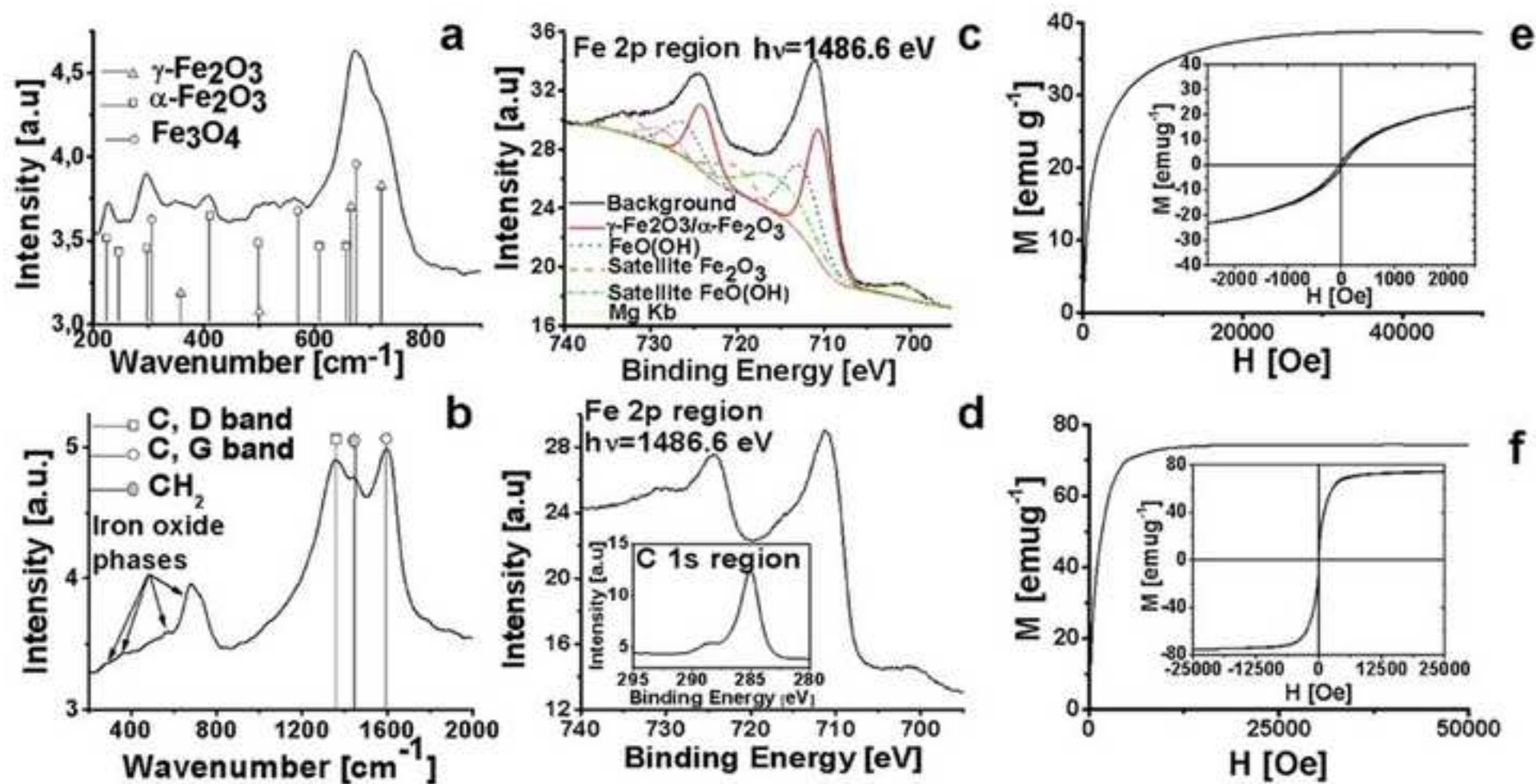
[Click here to download high resolution image](#)

Figure
[Click here to download high resolution image](#)

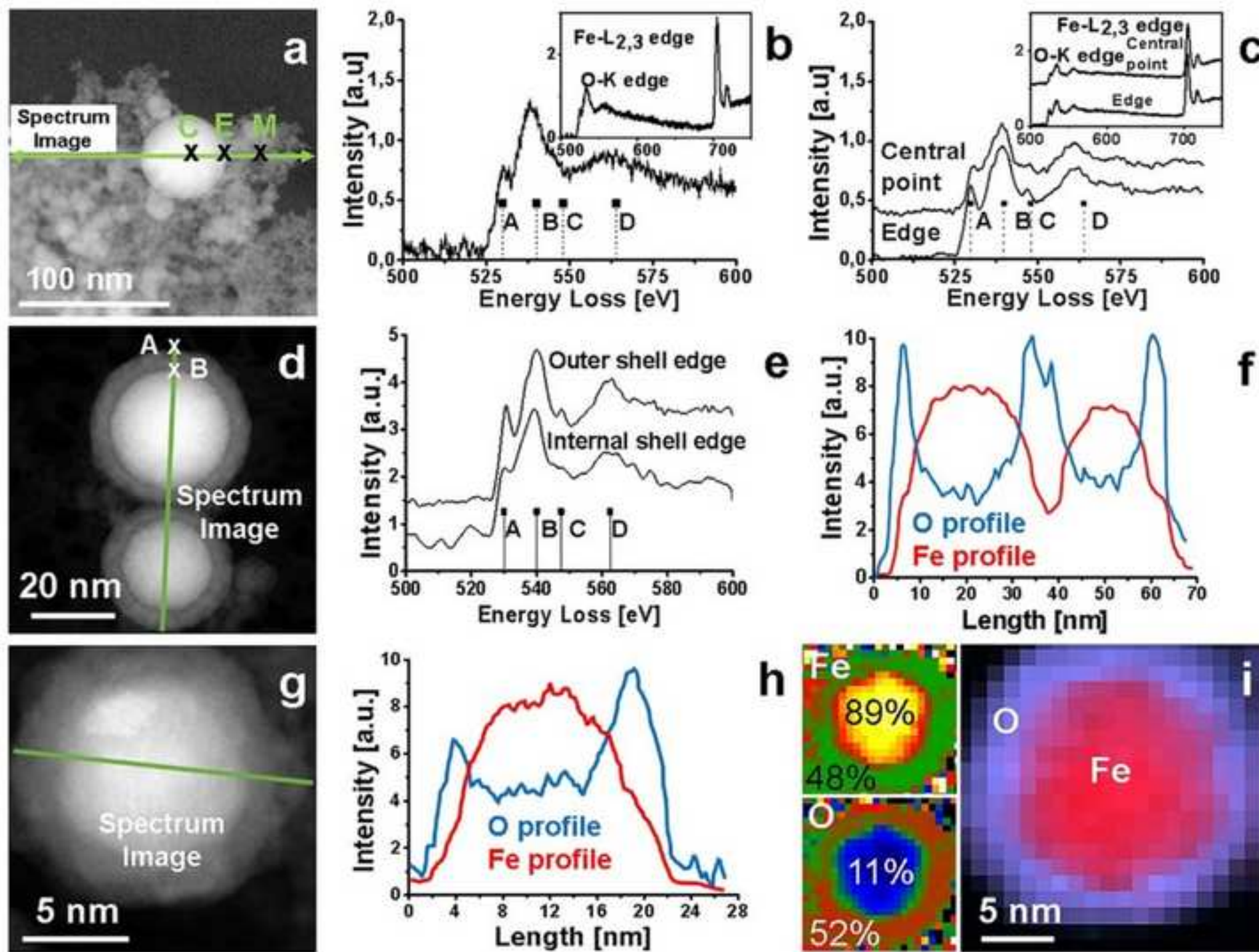
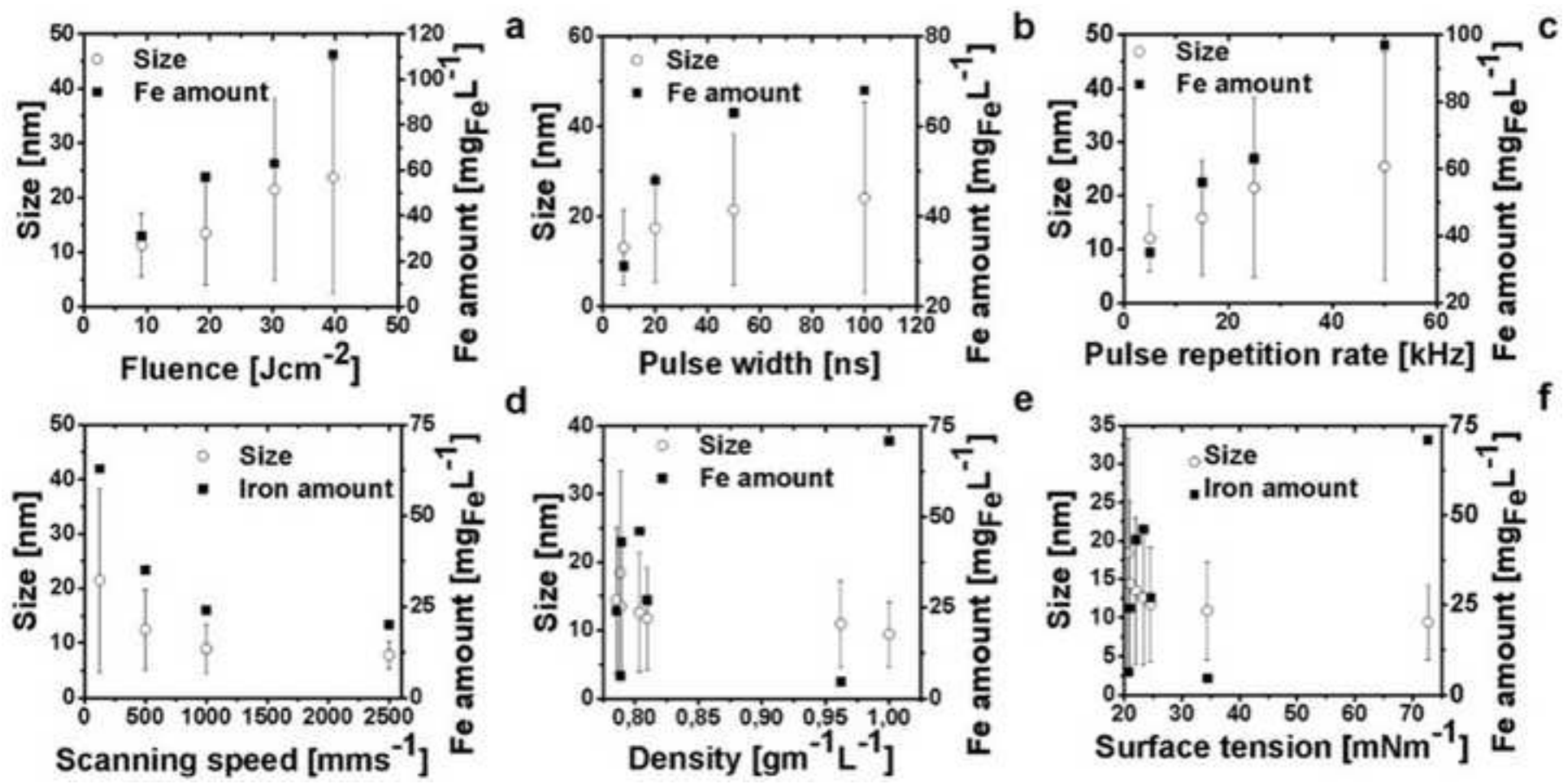


Figure
[Click here to download high resolution image](#)



Figure

[Click here to download high resolution image](#)

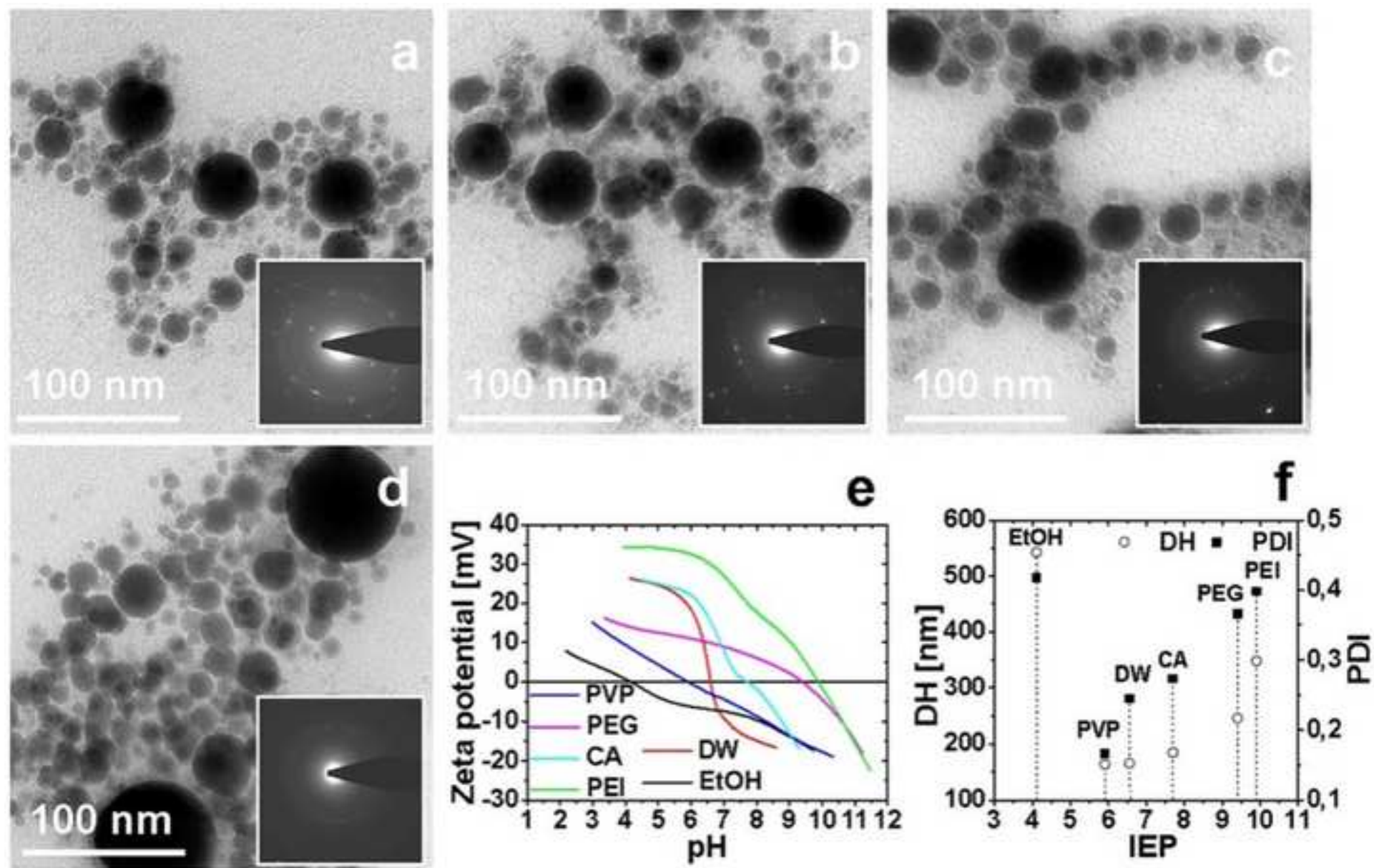


Table 1. Laser irradiation conditions used for the synthesis in pure distilled water (Sample 1) and ethanol (Samples 2-15), together with nanoparticle properties.

S ^{a)}	λ ^{b)} [nm]	P ^{c)} [W]	f ^{d)} [kHz]	τ_p ^{e)} [ns]	E _p ^{f)} [mJ]	F ^{g)} [J·cm ⁻²]	v _s ^{h)} [mm·s ⁻¹]	N ⁱ⁾	D _{TEM} ^{j)} [nm]	Sd _{TEM} ^{k)} [nm]	PDI ^{l)}	Ablation rate [mg _{Fe} L ⁻¹ h ⁻¹]	Fe content [mg _{Fe} ·mL ⁻¹]
1	1050	3.42	25	50	0.137	19.35	125	6.0	9.4	4.8	0.26	681	95
2	1050	3.42	25	50	0.137	19.35	125	6.0	13.5	9.5	0.50	408	57
3	532	3.42	25	50	0.137	19.35	125	6.0	12.4	9.2	0.54	466	65
4	1050	1.62	25	50	0.065	9.17	125	6.0	11.2	5.9	0.27	222	31
5	1050	5.35	25	50	0.214	30.28	125	6.0	21.5	16.8	0.61	452	63
6	1050	7.0	25	50	0.280	39.61	125	6.0	23.7	21.3	0.81	796	111
7	1050	5.35	25	8	0.214	30.28	125	6.0	13.1	8.4	0.41	208	29
8	1050	5.35	25	20	0.214	30.28	125	6.0	17.4	11.9	0.47	344	48
9	1050	5.35	25	100	0.214	30.38	125	6.0	24.1	21.3	0.78	488	68
10	1050	5.35	5	50	1.07	151.38	125	1.2	12.1	6.2	0.27	251	35
11	1050	5.35	15	50	0.356	50.46	125	3.6	15.8	10.8	0.46	402	56
12	1050	5.35	50	50	0.107	15.14	125	12	25.4	21.3	0.70	696	97
13	1050	5.35	25	50	0.214	30.28	500	1.5	12.4	7.4	0.35	251	35
14	1050	5.35	25	50	0.214	30.28	1000	0.8	8.9	4.4	0.25	172	24
15	1050	5.35	25	50	0.214	30.28	2500	0.3	7.8	2.5	0.10	143	20

a) sample; b) laser wavelength; c) power of the laser beam; d) pulse repetition rate; e) pulse width; f) average pulse energy; g) pulse fluence; h) scanning speed; i) pulse accumulation per spot; j) mean diameter obtained by TEM analysis; k) standard deviation; l) overall polydispersity index.

Table 2. Relevant physical properties at 25°C of the solvents used as ablation media, together with nanoparticle properties. [42]

S ^{a)}	Solvent	$\delta^{b)}$ [g·mL ⁻¹]	$\sigma^{c)}$ [mN·m ⁻¹]	D _{TEM} ^{d)} [nm]	Sd _{TEM} ^{e)} [nm]	PDI ^{f)}	Dry weight [mg·L ⁻¹]	Fe content [mg _{Fe} ·mL ⁻¹]
1	Water (H ₂ O)	1.0	72.70	9.4	4.8	0.26	177	95
2	Ethanol (C ₂ H ₆ O)	0.7892	21.97	13.5	9.5	0.50	51	57
16	1-Propanol (C ₃ H ₈ O)	0.8037	23.30	12.6	8.7	0.47	80	46
17	2-Propanol (C ₃ H ₈ O)	0.7854	20.93	14.4	10.8	0.57	68	24
18	1-Butanol (C ₄ H ₁₀ O)	0.8097	24.57	11.7	7.4	0.40	269	27
19	tert-Butanol (C ₄ H ₁₀ O)	0.7886	20.70	18.4	14.9	0.66	277	6.3
20	Cyclohexanol (C ₆ H ₁₂ O)	0.962	34.40	10.9	6.3	0.33	286	4.6

a) sample; b) density; c) surface tension; d) mean diameter obtained by TEM analysis; e) standard deviation; f) overall polydispersity index.